

GAUSSIAN DECONVOLUTION OF 21 CM HI SPECTRA

by

MARCUS ALEXANDER

(Under the Direction of Loris Magnani)

ABSTRACT

This work investigates atomic hydrogen emission line spectra at 1420 MHz from the 100 meter Green Bank Telescope in Green Bank, West Virginia using the technique of Gaussian deconvolution. Data from the Green Bank Telescope is superior to data previously used in Gaussian deconvolution studies as the Green Bank Telescope minimizes side lobe radiation, producing some of the purest 21 cm spectra to date.

The results show evidence for the components of the Cold Neutral Medium, Warm Neutral Medium, and a third, broad component previously hypothesized to be due to instrumental effects. The nature of the broad component is discussed, and we conclude that the broad component can be produced by a combination of Cold and Warm Neutral Medium emission regions, and Galactic streaming and noncircular motions.

INDEX WORDS: Interstellar Medium, Atomic Hydrogen, Cold Neutral Medium, Warm Neutral Medium, Galactic Rotation

GAUSSIAN DECONVOLUTION OF 21 CM HI SPECTRA

by

MARCUS ALEXANDER

B.S., The University of Georgia, 2006

A Thesis Submitted to the Graduate Faculty of The University of Georgia in Partial Fulfillment
of the Requirements for the Degree

MASTER OF SCIENCE

ATHENS, GEORGIA

2008

© 2008

Marcus Alexander

All Rights Reserved

GAUSSIAN DECONVOLUTION OF 21 CM HI SPECTRA

by

MARCUS ALEXANDER

Major Professor: Loris Magnani

Committee: Jean-Pierre Caillault
Robin L. Shelton

Electronic Version Approved:

Maureen Grasso
Dean of the Graduate School
The University of Georgia
December 2008

TABLE OF CONTENTS

CHAPTER	Page
1 INTRODUCTION.....	1
1.1 The Interstellar Medium.....	1
1.2 The Phases of the Interstellar Medium.....	6
1.3 The Stability Criteria.....	9
1.4 Models for the Phases of the ISM.....	12
1.5 Observational Signatures of the CNM/WNM.....	14
1.6 Summary of Thesis.....	16
2 GAUSSIAN DECONVOLUTION OF HI PROFILES.....	17
2.1 Line Broadening Mechanisms.....	17
2.2 The Gaussian Deconvolution Technique.....	19
2.3 Problems With the Technique.....	20
2.4 Previous Work.....	27
3 THE OBSERVATIONS.....	30
3.1 The HI Drift Scan Survey.....	30
3.2 High Velocity Clouds.....	36
4 RESULTS.....	44
5 DISCUSSION.....	58
6 CONCLUSION.....	61

REFERENCES.....	63
-----------------	----

Chapter 1

INTRODUCTION

1.1 THE INTERSTELLAR MEDIUM

The interstellar medium (ISM) is the baryonic matter in a galaxy distributed between the stellar component. The ISM is comprised of gas (99% by mass) and dust (1%). In this thesis, we will focus primarily on the gas which is made up of approximately 90% hydrogen and 10% helium by the number of nuclei, with trace amounts of heavier elements. The hydrogen gas that dominates the mass balance of the ISM assumes many different temperature and density configurations each of which occupies varying volumes in different regions of the galaxy. These configurations are often referred to as “phases”. The molecular phase plays a key role in the evolution of the Galaxy because some of this gas can eventually form stars. In this way, the gas of the ISM and the stellar component are intertwined. In essence, the gas found in the ISM is part of the so-called star-gas cycle, shown in detail in Figure 1-1. A portion of the atomic gas turns molecular, and under certain conditions a portion of the molecular gas forms stars. These stars undergo fusion for millions to billions of years before dying and releasing most of their gas back into the ISM to continue the cycle. The star-gas cycle is a key component for understanding the Galaxy and so any understanding of the evolution of galaxies depends on fully understanding all steps in this cycle. In this thesis we will focus on the atomic hydrogen component of the ISM.

The atomic component can be either neutral or ionized. The neutral component dominates

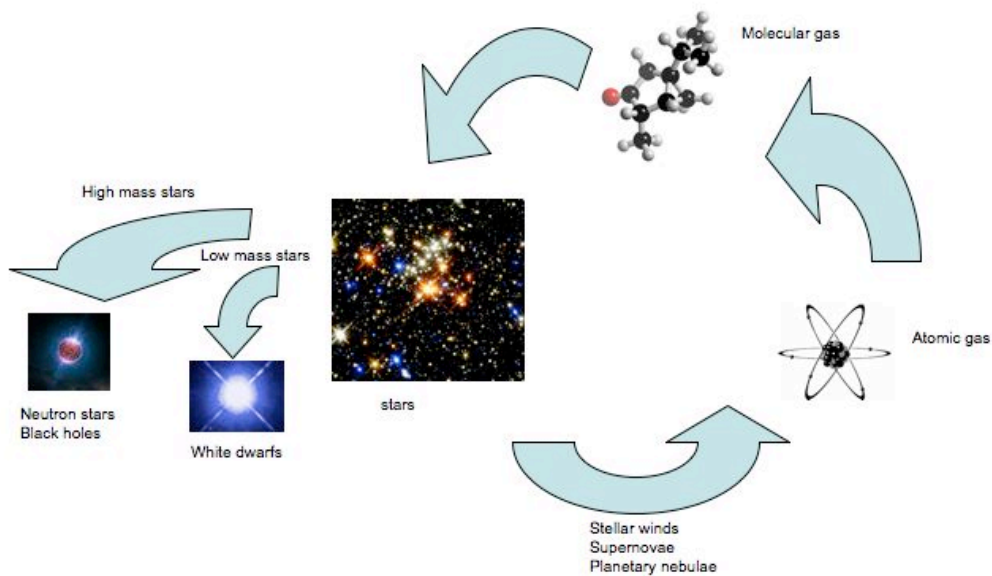


Figure 1-1. The star-gas cycle. Stars form from molecular clouds and as they evolve and die they recycle up to 80% of their material back into the interstellar medium. A portion of this gas cools into neutral hydrogen at different temperatures and densities (see text). About half of the neutral hydrogen eventually becomes molecular and the cycle continues. The compact end products of stellar evolution (white dwarfs, neutron stars, and black holes) are removed from the cycle and constitute the “waste products” of this cycle.

by mass with an estimated $4.8 \times 10^9 M_{\odot}$ of atomic hydrogen (HI)¹, and Galactic HI makes up about 4% of the mass of the baryonic matter (Bahcall et al. 1983). Estimates for the total amount of H₂ vary from $1.2 \times 10^9 M_{\odot}$ to $3.5 \times 10^9 M_{\odot}$ (Sanders et al. 1984). However, the HI and H₂ are distributed differently in the Galactic plane: the mean surface density distribution of HI is nearly constant from 4 kpc to 20 kpc. In contrast, the H₂ is strongly peaked at the Galactic center, peaking again (though at a value a factor of 15 less) at 4-6 kpc, and then decreasing markedly beyond 8 kpc (See Scoville 1987 for details). Thus, the HI distribution dominates H₂ in mass beyond the Solar Circle (the radius of the Sun's orbit around the Galactic Center); moreover, the HI is not exclusively concentrated in distinct, isolated, giant clouds like H₂. A portion of the HI is broadly distributed and there is no line of sight where the Galactic HI 21 cm line cannot be detected (i.e., the surface filling factor is 1.0). The estimates of how much Galactic interstellar space is filled with neutral hydrogen, the volume filling factor, range greatly from 20% to 90% (Kulkarni and Heiles 1988) and the question has never satisfactorily been resolved (See review by Cox 2005).

The neutral medium of the Galaxy is organized in a cool, clumped diffuse HI phase (≈ 100 K) known as the Cold Neutral Medium (CNM) and warm, distributed gas (≈ 8000 K) known as the Warm Neutral Medium (WNM). The density of the CNM is typically 50 cm^{-3} while the density of the WNM is about 0.5 cm^{-3} . It is thus clear that the two phases are approximately in pressure equilibrium.

The neutral atomic gas is primarily traced by the 21 cm line of atomic hydrogen at 1420.406 MHz produced by the spin-flip transition of hydrogen. Both the proton and the electron in a hydrogen atom have an intrinsic, quantized angular momentum called "spin", and when the spins

¹ Astronomers refer to neutral hydrogen as HI, and ionized hydrogen as HII.

are in the same direction the atom has a slightly higher energy than if they were in opposing directions. The higher energy state is excited by collisions with electrons and other atoms. Eventually (typically, the lifetime of the state is 12 million years), the electron will spontaneously flip its spin back to the lower energy configuration. When this happens, a photon is emitted with the energy equivalent to the difference between the two spin states of the hydrogen atom. It may seem that this spin-flip occurs too rarely to produce a significant spectral line, but the sheer number of neutral hydrogen atoms along any line of sight in the Galaxy ensures that the 21 cm line is easily detected and is the strongest non-masing spectral line in the ISM.

The ionized gas itself is also divided into two phases. The warm ionized medium (WIM) is around the same temperature as the WNM (≈ 8000 K), but at a somewhat lower density (≈ 0.1 cm^{-3}). Since the gas is ionized, there is not an electron to produce the spin-flip transition. Therefore, the WIM has to be traced through other methods; typically the dispersion of pulsar signals, optical and UV ionic absorption lines observed against background sources, and emission in the $\text{H}\alpha$ recombination line (Reynolds 1987).

Gas with temperatures on the order of 10^5 - 10^6 K is fully ionized and is considered to be part of the Hot Ionized Medium (HIM). This gas is traced mainly through UV absorption lines of highly ionized molecules, but the gas also emits continuum and line radiation in the far UV and X-ray regions. Observations from space satellites have shown the existence of a pervasive HIM that has low density ($\approx 10^{-3}$ cm^{-3}) with temperatures ranging from 3×10^5 to 1×10^6 K. The gas is heated through shocks in the ISM driven by stellar winds from early type stars as well as supernova explosions (see, e.g., Savage 1987). The volume filling factor of this phase is also still highly controversial (Cox 2005).

Molecular gas is significantly more dense than atomic gas, and it is most commonly traced by the J=1-0 transition in carbon monoxide (CO) with a characteristic wavelength of 2.6 mm. Galactic surveys in this line have shown that much of the gas resides in large, distinct entities known as “clouds” with typical densities $> 200 \text{ cm}^{-3}$ and temperatures of 10 K (Combes 1991). While these are characteristic values, molecular clouds show large ranges of temperature and densities (Goldsmith 1987). Unlike other phases in the ISM, molecular gas is mostly gravitationally bound, meaning the clouds are self-gravitating. These clouds are dominated by turbulent pressures indicated by suprathermal line-broadening in the emission lines. Most of them are stable over long time scales (on the order of 10^7 years) due to a balance between magnetic pressure, turbulent pressure, and gravity. Because these clouds are gravitationally bound, they are the sites of all star formation in the Galaxy (Smith 2004). Observations have shown that molecular clouds have spatial structure on all scales. This includes cores on the order of ≈ 0.1 pc, with densities on the order of 10^4 cm^{-3} or greater, and large molecular complexes with masses in the range of 10^4 - $10^6 M_{\odot}$ where localized star formation (both large and small) occurs.

In addition to the gas in the ISM there is also a dust component. Though only $\approx 1\%$ of the gas mass, the dust component is relatively easy to trace via thermal infrared emission and is studied intensively (Whittet 2003). Interstellar dust shows up in the ISM in various ways. Small dust grains will absorb and scatter light from distant stars, providing a general reddening and extinction to the observed starlight. Large, elongated dust grains aligned in the galactic magnetic field cause the observed starlight to be polarized. If the dust is near a bright star, the scattering of starlight from the dust will produce a reflection nebula. Cold dust (15-20 K) grains produce thermal emission peaking at $145 - 190 \mu\text{m}$, making the ISM as a whole bright in the infrared, a

fact exploited by the Infrared Astronomy Telescope (IRAS) (Low et al. 1984) and Spitzer Space Telescope (Werner et al. 2006) missions.

1.2 THE PHASES OF THE INTERSTELLAR MEDIUM

The cold neutral medium (CNM) and the warm neutral medium (WNM) are thought to exist side-by-side in thermal and pressure equilibrium (See, e.g. Cox 2005). The ISM is heated primarily by diffuse starlight and cosmic rays whereas cooling occurs through radiation losses. Excitation of the fine-structure level of ionized carbon (CII) dominates the cooling at the low temperatures of the CNM (≈ 100 K). For the WNM, there exists a balance of heating with cooling processes such as visible transitions of oxygen and hydrogen's Lyman α . For this lower density WNM gas, the balance between heating and cooling results in a temperature of 5,000-10,000 K. However, whether these phases are stable depends on examining stability criteria (see below).

If both phases are present, the high temperature phase must have a lower density if it is to be in pressure equilibrium with the cooler phase. Considering the maximum efficiency of the photo-electric effect on polycyclic aromatic hydrocarbons (PAHs) and small dust grains, CII cooling can balance the heating from electron collisions but only for densities greater than ≈ 20 cm^{-3} . For densities lower than ≈ 20 cm^{-3} , other cooling processes must contribute or the photoelectric heating efficiency should be less due to charging effects on the grains or PAHs (Tielens 2005).

In order to understand why the atomic ISM organizes itself in phases, consider the gas cooling function Λ and the gas heating rate Γ . The net cooling (in $\text{ergs s}^{-1} \text{gm}^{-1}$) is defined by the generalized loss function, \mathcal{L} ,

$$\mathcal{E} \equiv n^2\Lambda - n\Gamma.$$

where the dependence on the particle volume density (n , in units of cm^{-3}) for both the cooling and heating terms is shown explicitly. Generally, since Λ and Γ depend on the physical conditions (n and T) of the medium, so does \mathcal{E} . For $\mathcal{E} > 0$ the gas is cooling down, and for $\mathcal{E} < 0$ the gas is heating up. When $\mathcal{E} = 0$, the resulting curve in the n - T plane defines thermal equilibrium. We can write this condition as

$$n\Gamma = n^2\Lambda.$$

In this formulation, Λ is independent of the density, and in the low density limit this can be rewritten as

$$(\Gamma/nkT) = (\Lambda/kT).$$

Here, k is the Boltzmann constant. Because the right-hand side of the equation depends only on the temperature and the left side can be expressed as Γ/P , it is natural to plot $\log(\Gamma/P)$ vs. $\log T$ (see Figure 1-2). The locus of the thermal equilibrium curve can be found where $\mathcal{E} = 0$ on the diagram. Points above the curve are where heating exceeds cooling (i.e. where $\mathcal{E} < 0$), while below the curve cooling exceeds heating. Assuming the heating comes from cosmic rays, heating is independent of density. This leads to constant heating rates at constant pressure, value of Γ/P the ISM can have specific values of n and T . For reasonable values of Γ/P in the corresponding to a value of Γ/P shown as a horizontal line on the curve in Figure 1-2. Where the horizontal line and the cooling curve meet are equilibrium points, regions where for a given Galaxy, there are four equilibrium points; two stable and two unstable (they are clearly marked in Figure 1-2). For the two unstable points, small perturbations in n and/or T will move the gas parameters away from these values corresponding to the equilibrium locations on the curve.

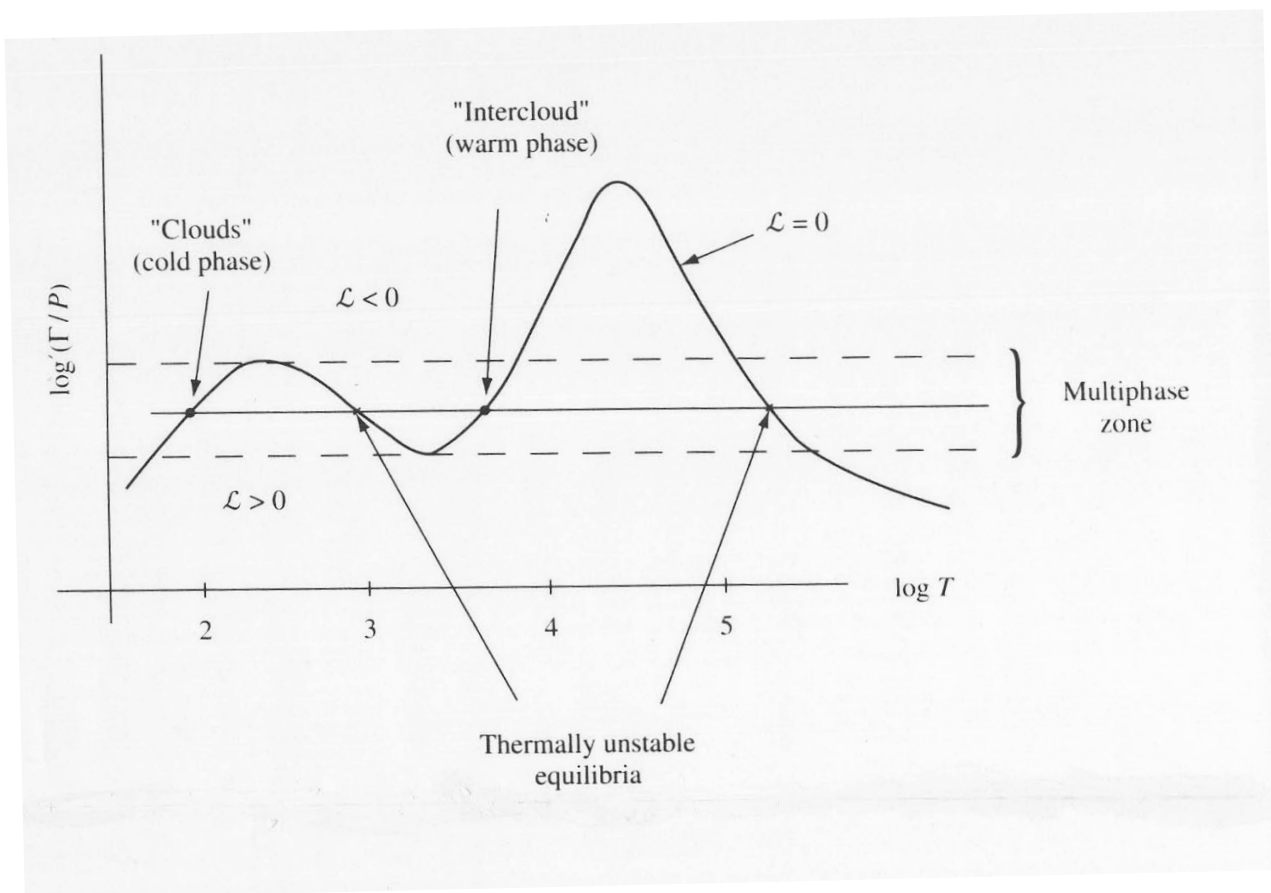


Figure 1-2. The thermal equilibrium curve (the curve with $\mathcal{L}=0$) in a plot of $\log(\Gamma/P)$ vs. $\log T$. The equilibrium points are marked at the intersection of the line for a constant value of $\log(\Gamma/P)$ and the thermal equilibrium curve. See sections 1.2 and 1.3 for details. Figure taken from "Interstellar Processes", Eds. D. J. Hollenbach and H. A. Thronson, Jr. (1987), Panel Discussion: Phases of the Interstellar Medium, J. M. Shull, p. 225. © 1987 by D. Reidel Publishing Company. With kind permission of Springer Science and Business Media.

The shape of the $\xi=0$ curve is determined by the cooling curve, a plot of $\ln \Lambda$ vs. $\ln T$ (see Figure 1-3). The cooling curve, which can be calculated if one knows the abundance of the various elements in the ISM (and the relevant physical processes that produce radiative energy loss), can be used to calculate the function Λ/T which is proportional to Γ/P . Determining the value of Λ/T for a given T leads to a point on the $\xi=0$ curve. The locus of all such points results in the curve shown in Figure 1-2.

The criteria for determining which equilibrium points are stable and unstable are described in the next section. The two stable points correspond to the n and T values of the CNM and WNM. If the pressure of the ISM drops below a minimum pressure, only the WNM remains, whereas at high pressures only the CNM remains. In summary, the existence of these two phases in pressure and thermal equilibrium is a natural consequence of the cooling curve of the gas.

1.3 THE STABILITY CRITERIA

Stability of the equilibrium points described above is tested for by introducing a perturbation in density such that a thermodynamic variable (e.g. pressure) is held constant. If atomic gas has values of n and T typical of one of the equilibrium points, then instability results if, for example, near the equilibrium point with highest T the radiation losses increase with decreasing temperature. If this is the case, a cooler than average region cools more effectively than its surroundings. More specifically, in the case of the generalized loss function, if decreases (i.e., ΔT is negative) $\Delta \xi$ is positive which means it is cooling, but at a greater rate. This, in turn, makes ΔT decrease even more strongly leading to a runaway. In general, the gas will be thermally unstable if the change in ξ is opposite in sign to the change in entropy, S (Field 1965). In other words, for a thermodynamic variable A , the temperature

$$(\partial\mathcal{F}/\partial S)_A < 0$$

where the notation means $(\partial\mathcal{F}/\partial S)$ evaluated at constant A. More particularly, the stability criterion for isochoric perturbations quoted by Field (1965) is $(\partial\mathcal{F}/\partial T)_\rho < 0$, where ρ is density, and for isobaric perturbations

$$(\partial\mathcal{F}/\partial T)_P = (\partial\mathcal{F}/\partial T)_\rho - (\rho_0/T_0) (\partial\mathcal{F}/\partial\rho)_T < 0.$$

The isobaric stability criterion can be rewritten as $d(\ln \Lambda)/d(\ln T) < 1$. With this version of the instability criterion, instability occurs wherever the cooling curve (Figure 1-3) is *not* steeply rising. In contrast, stability occurs wherever the cooling curve is steeply rising. As Figure 3 shows, this occurs at ≈ 100 K and $\approx 10,000$ K. Thus the stable phases are at these temperatures and correspond to the CNM and WNM.

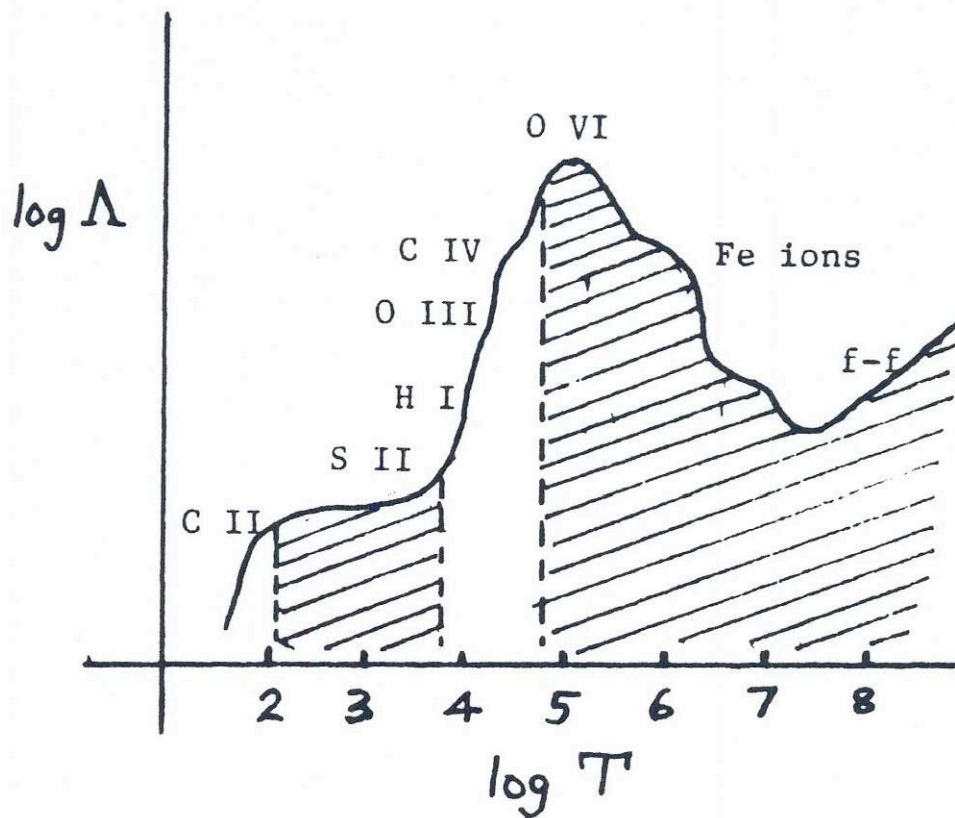


Figure 1-3. The cooling curve. Stability occurs wherever the curve is steeply rising, i.e. between a $\log T$ of 1-2 and 4-5. See section 1.3 for details. Figure taken from “Interstellar Processes”, Eds. D.J. Hollenbach and H.A. Thronson, Jr. (1987), Panel Discussion: Phases of the Interstellar Medium, J. M. Shull, p. 225. © 1987 by D. Reidel Publishing Company. With kind permission of Springer Science and Business Media.

1.4 MODELS FOR THE PHASES OF THE ISM

Models for the ISM involving the CNM and the WNM were referred to as “two-phase” models and were developed in the late 1960s. The first successful model was proposed by Field, Goldsmith, and Habing (1969). Their model was based on cold atomic clouds in a warm soup of HI, and adopted a high cosmic-ray ionization and heating rate ($\zeta_{\text{CR}} \approx 10^{-15} \text{ s}^{-1}$). Since then, molecular observations and astrochemical models of the clouds have shown that the ISM cosmic-ray ionization rate is an order of magnitude lower than assumed by Field, Goldsmith, and Habing. Thus, it turns out that cosmic rays are not important to the energy balance on a larger scale (Tielens 2005). Other heating processes were considered over the years, including X-rays and dissipation of Alfvén waves. Currently, the favored mechanism is photoelectric heating with the electrons ejected primarily from large molecules likely to be PAHs or small dust grains (Lepp and Dalgarno 1988; Bakes and Tielens 1990).

McKee and Ostriker (1977) developed a supernova remnant-dominated model for the interstellar medium consisting of three phases, two being the cold and warm components and the third composed of hot (10^6 K) cavities occupying most of the volume. In their model, the HI mass is concentrated in clouds with the cores of these clouds being cold and neutral, surrounded by warm envelopes. The cloud envelopes occupy more volume than the than the cloud cores, but the cores have far more mass than the envelopes (the volume filling factor of the envelopes is 38%, but only 4% of the mass is in the envelopes). The volume filling factors for the components in this model are $f_{\text{cold}} \approx 0.025$, $f_{\text{warm}} \approx 0.38$, and $f_{\text{hot}} \approx 0.6$.

There were several successful predictions from this “three-phase” model including the average interstellar pressure $nT \approx 3700 \text{ cm}^{-3} \text{ K}$, and electron densities from the WIM cloud envelopes, $\langle n_e \rangle = 0.04 \text{ cm}^{-3}$ and $\langle n_e^2 \rangle^{1/2} = 0.08 \text{ cm}^{-3}$, which are values near those found through

pulsar dispersion measures (for CNM clouds). Other successful predictions include the observed HI cloud velocity dispersion $\langle V_{cl} \rangle \approx 8 \text{ km s}^{-1}$ and the soft X-ray intensities in the Local Bubble.

Whatever the true nature of the ISM, there is still ample need for observational constraints on the various theories and models. Although the three-phase model is a big step forward (because of the inclusion of supernovae and supernova remnants) and made several successful predictions, it did fail in several respects. These are described in detail by Cox (2005). We list them here briefly: Firstly, the presence of small CNM clouds whose fate is to be evaporated by the hot gas in the HIM. The actual CNM structures observed to exist in the ISM appear to be very different in size and geometry from the small, compact clouds described by McKee and Ostriker (Heiles and Toland 2003). Secondly, the confining effect of magnetic fields is not considered, despite clear effects on the evolution of expanding bubbles (Raley, E. A., Shelton, R. L., Plewa T. 2007) Thirdly, evaporation of CNM cloudlets is the mechanism McKee and Ostriker use to transfer gas into the WNM, whereas Cox (2005) favors thermal conduction. Fourthly, their model vastly overestimates the amount of OVI present in the hot phase. Finally, the sizes of the supernova cavities in the three-phase model are enormous compared to observations.

In summary, though the gross behavior of the ISM is reproduced by the McKee-Ostriker model, many inconsistencies with observations and physical details need to be worked out. The review article by Cox (2005) concludes with several different conceptions of the large-scale properties of the ISM and proposes a “polymeric” view of the ISM. In this picture, the magnetic field plays the part of the strands of an elastic polymer threading through and confining the various gas components with the whole galactic plane distribution confined by a buoyant hot halo. Given the very different pictures of what the local ISM is like, the need for more observational constraints is clear.

1.5 OBSERVATIONAL SIGNATURES OF THE CNM/WNM

The WNM and CNM are primarily detected via emission and absorption spectra of the 21 cm HI line (See reviews by Kulkarni and Heiles 1988 and Dickey and Lockman 1990). Typical emission and absorption spectra are shown in Radhakrishnan et al (1972). These authors made observations towards extragalactic continuum sources using single-dish radio telescopes and interferometry. The former revealed emission profiles consisting of both narrow and broad components, while the latter showed only narrow absorption components. The narrow emission components have associated absorption features detected via interferometric observations of extragalactic continuum sources indicating that the gas is relatively dense (Kulkarni and Heiles 1987). In contrast, the broad components do not have associated absorption features implying that the gas producing the broad emission component is not very dense. Since the opacity is inversely proportional to the spin temperature, T_s , which is close to the kinetic temperature for HI, the narrow components represent the CNM while the wide components represent the WNM. The classic emission-absorption HI experiments by Radhakrishnan et al. (1972) established the existence of the WNM and gave observational support to at least the CNM and WNM aspects of both the two-phase and three-phase models of the ISM.

Although the emission-absorption observations by Radhakrishnan et al. (1972) and Payne, Salpeter, and Terzian (1983) demonstrated conclusively the existence of the WNM, there is another technique that can be used to study this component: Gaussian deconvolution of spectral profiles.

Mebold (1972) decomposed about 1300 HI emission spectra into narrow and wide Gaussian components. He found the wide- σ_v^2 HI has a scale height of about 200 pc and an intrinsic velocity dispersion of about 8.8 km s^{-1} , corresponding to a WNM with an upper limit temperature of 9600 K. He also found that the narrow- σ_v HI was probably due to isolated nearby clouds and has a velocity dispersion of 3 km s^{-1} or less, depending on the diameter of the radio telescope antenna beam. Mebold's technique of Gaussian deconvolution will be discussed in detail in Section 2 because, in this thesis, we use that method to study the temperature distribution of the CNM and WNM.

After Mebold's work, Verschuur and Schmelz (1989) and Verschuur and Magnani (1994) applied the same technique to 21 cm spectra from Arecibo. Verschuur and Schmelz (1989) confirmed the existence of the CNM; Verschuur and Magnani (1994), like Mebold (1972), identified both narrow and wide HI components in their sample of spectra. In addition, they identified a third, very wide component which, if interpreted solely in terms of the thermal motion, would result in the absurd temperature for a neutral component of 24,000 K. These authors could not determine whether this component (somewhat inconveniently dubbed "Component 1") was attributable to 21 cm emission (regardless of how to interpret the width) or to instrumental effects such as stray radiation. More importantly, the previously seen wide component (dubbed "component 2" by Verschuur and Magnani 1994) resulted in temperatures for the WNM substantially lower than those reported by Mebold (1972): 3,000 K for Verschuur and collaborators vs. 9,400 K for Mebold. In their review article, Kulkarni and Heiles (1988) discuss the need for more extensive studies of the temperature of the WNM.

² σ_v is the velocity dispersion of the various 21 cm components that comprise the spectral line. For a Gaussian fit, $\sigma_v = \text{FWHM (Full Width at Half Maximum of the spectral line)} / 2.35$

In order to address that need, and to determine whether component 1 is “real” or not, we performed Gaussian deconvolution on over 5,000 spectra from the NRAO 100 meter Green Bank Telescope in West Virginia³. In the remainder of this thesis we describe our technique, data, and results.

1.6 SUMMARY OF THESIS

In Chapter 2 we will discuss the technique of Gaussian de-convolution in detail, some of the pitfalls associated with the procedure, and previous work in this area. Chapter 3 describes our observations and the HI data set from the 100 m Green Bank Telescope. In Chapter 4 we describe the basic results of our analysis. We identify the existence of a CNM, a WNM, and an even broader component whose nature has not been determined. In Chapter 5 we discuss each of these three components and speculate on the origin of the very wide component. In the concluding chapter we summarize our findings and describe avenues for further work in this area.

³ The National Radio Astronomy Observatory (NRAO) is operated by Associated Universities, Inc., under contract with the National Science Foundation.

Chapter 2

GAUSSIAN DECONVOLUTION OF H_I PROFILES

2.1 LINE BROADENING MECHANISMS

Spectral lines can be broadened by different physical processes, some intrinsic to the atom or molecule, some extrinsic. A spread in energy to a given atomic or molecular energy level is produced by the Heisenberg uncertainty principle, where the spread in energy, ΔE , and the duration in the state, Δt , must satisfy $\Delta E \Delta t \approx h$. The line profile, $\Phi(\nu)$, produced by natural line broadening is described by

$$\Phi(\nu) = (\gamma/4\pi^2)/[(\nu-\nu_0)^2 + (\gamma/4\pi)^2]$$

where γ is the width parameter which is equal to the rate of spontaneous emission out of the line (the Einstein A coefficient), and ν_0 is the rest frequency of the transition. This applies to cases where only the upper state is broadened. If both the upper and lower states are broadened, then $\gamma = \gamma_u + \gamma_l$ where γ_u and γ_l are the widths of the upper and lower states in the transition.

If an atom suffers collisions while it is emitting, the phase of the emitted radiation can be altered very suddenly. The information about the emitting frequencies can be lost if the phase is altered completely randomly at the time of the collisions. If ν_{col} is the frequency of collisions, then the profile is given by

$$\Phi(\nu) = (\gamma + 2\nu_{col}/4\pi^2)/[(\nu-\nu_0)^2 + (\gamma/4\pi)^2].$$

However, the simplest mechanism for line broadening is produced by the Doppler effect. In a gas with a thermal distribution of velocities, each atom has its own Doppler shift. Although the total strength of the signal is not changed, the net effect is to spread the line in width. The

associated change in frequency of an atom with velocity component x (with the x -direction being along the line of sight) is, to lowest order in v/c ,

$$\nu - \nu_0 = \nu_0 v_x / c$$

where ν_0 is the frequency of the rest frame. The number of atoms with velocities between v_x and $v_x + dv_x$ is proportional to

$$\exp(-m_a v_x^2 / 2kT) dv_x,$$

the Maxwellian distribution where m_a is the mass of an atom and k is Boltzmann's constant, 1.38×10^{-16} erg/K. From the above equations we can clearly see that

$$v_x = c(\nu - \nu_0) / \nu_0$$

$$dv_x = c d\nu / \nu_0$$

Therefore, in the emission frequency range ν to $\nu + d\nu$, the strength of the emission is proportional to

$$\exp[-m_a c^2 (\nu - \nu_0)^2 / 2\nu_0^2 kT] d\nu$$

and the line profile function is

$$\Phi(\nu) = [e^{-(\nu - \nu_0)^2 / (\Delta\nu_D)^2}] / \{\Delta\nu_D(\pi)^{1/2}\},$$

where $\Delta\nu_D$ is the Doppler width defined by

$$\Delta\nu_D = [\nu_0 / c] (2kT / m_a)^{1/2}.$$

The constant in the profile function formula, $1 / \{\Delta\nu_D \text{sqrt}(\pi)\}$, is determined by the normalization condition $\int \Phi(\nu) d\nu = 1$ under the assumption that $\Delta\nu_D \ll \nu_0$. An important case of Doppler broadening is produced by turbulent velocities associated with macroscopic velocity fields. For the case where the scale of the turbulence is small compared with a mean free path (and assuming the turbulent velocities have a Gaussian distributions), the motions can be accounted for by an effective Doppler width

$$\Delta v_D = [v_0/c] \sqrt{2kT/m_a + \xi^2},$$

with ξ the root mean-square measure of the turbulent velocities.

In the ISM, the Doppler broadening dominates the other two types of broadening. Given the $\exp(-\Delta v)^2$ dependence of the Doppler broadened line profile, a Gaussian function is appropriate to fit to the observed line shapes.

A Gaussian function is described by 3 parameters; the height, the width (usually either in terms of σ or the Full-Width at Half-Maximum, where $2.35\sigma = \text{FWHM}$), and the centroid (where the height of the Gaussian is located on the abscissa).

Given the turbulence present in the ISM, it is common for long path lengths through the Galaxy to cross several turbulent cells, each with distinct centroid velocity. The resulting profiles are thus composed of several over-lapping Gaussians where each Gaussian tracks a Doppler-broadened turbulent cell. If the Gaussians have centroids that are sufficiently separated, and the signal-to-noise of the data is high, then the profile can be deconvolved into its individual, constituent profiles, one for each cell along the line of sight.

2.2 THE GAUSSIAN DECONVOLUTION TECHNIQUE

The deconvolving of the profiles in our dataset (described in Chapter 3) was done with the `xgaussfit` program in IDL⁴. One must fit several Gaussian profiles to the signal until a best fit to the data in a least squares sense is achieved. Operationally, each time a profile is applied to the signal, it is subtracted so the remaining signal can be fitted (see Figure 2-1). This process continues until the residuals are more or less at the rms level of the non-signal parts of the spectrum. Once the signal has been fitted, the fitting statistics are calculated (height, width,

⁴ IDL is a programming language including many constructs from Fortran and C.

centroid) and presented to the fitter. The “Goodness of Fit” is a scalar representing how well the added Gaussians reproduce the given spectra. Also presented to the fitter are the residuals (or fitting errors) for the fitted profile. These are extremely useful because they not only show whether or not the fit is good, but discrepancies in the residuals show where there may be a problem with the fit. This can include features that the fitter may not have noticed in the original attempt to fit the profile. Based on the statistics given, one can choose to keep the fit and save it to a file or to start over and try again. The initial parameter choices for the first profile to be fit to data are subjective and the solution to the line profile in terms of the total number of Gaussians used to fit the line may not be unique – especially if the signal-to-noise level is low. We elaborate on this below.

2.3 PROBLEMS WITH THE TECHNIQUE

As with any procedure performed subjectively by a human being, problems can arise. It is possible for the same profile to be fitted with four Gaussians that produce good fitting statistics, as well as four different Gaussians (i.e., with different parameters) that also produce good fitting statistics. The case could also arise that the profile could be fitted with three or five Gaussians and still produce good fitting statistics, though obviously very different from those of a four Gaussian fit. However, our data is of very good quality with relatively high signal-to-noise (see Section 3). As described in Chapter 3, we add 4 spectra together to improve the rms by a factor of 2 to ~ 0.07 K. This is significantly better than the rms values of most HI surveys. Several test spectra were fitted by myself, Loris Magnani, and Ray Chastain for the purpose of comparing subjectivity of the fits and, in each case, virtually the same Gaussians and fitting statistics resulted. Verschuur and Schmeltz (1989) also discuss this issue and conclude that with few

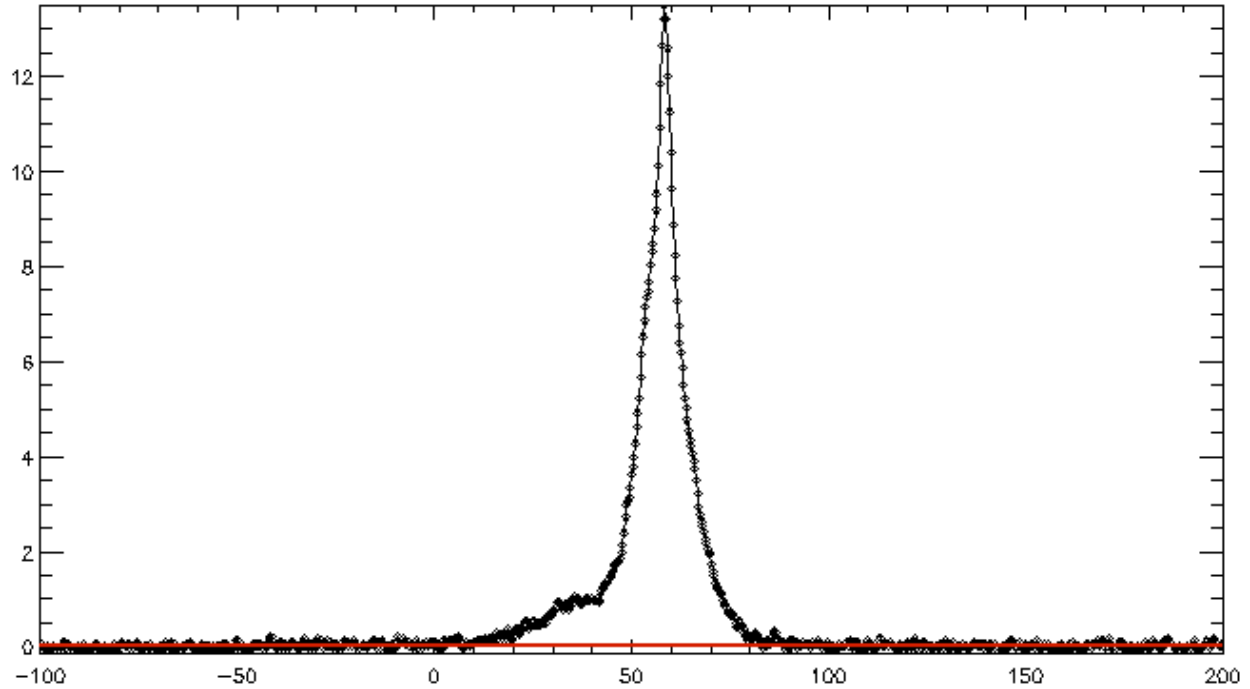


Figure 2-1a. A typical 21-cm HI emission spectra from the data set. The spectrum is produced by adding four spectra at positions $(l,b) = (219.78^\circ, 46.67^\circ), (219.80^\circ, 46.70^\circ), (219.82^\circ, 46.74^\circ), (219.85^\circ, 46.78^\circ)$. The x-axis is the velocity in units of km/s and the y-axis is the antenna temperature in units of K.

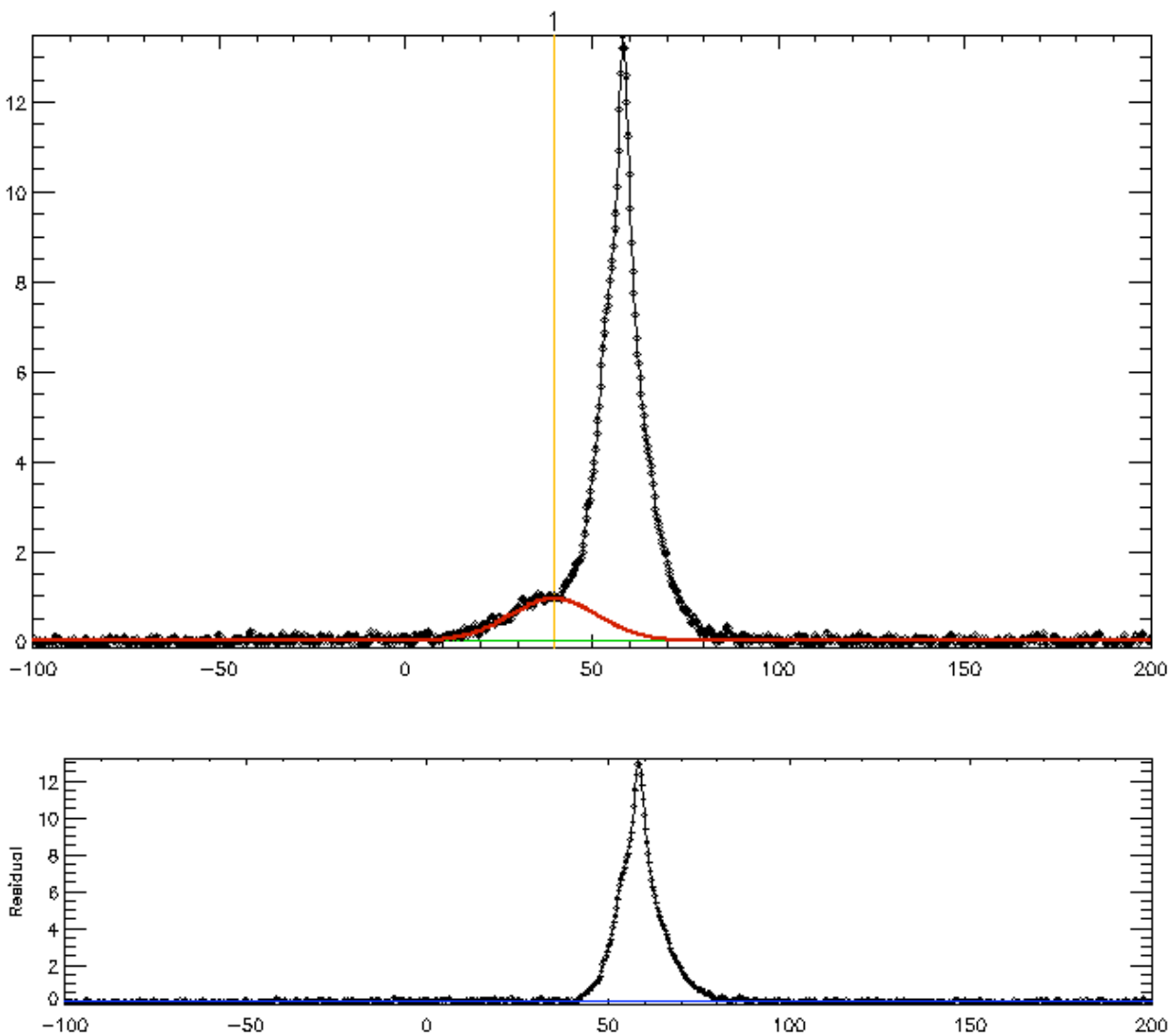


Figure 2-1b. The same spectrum as in Figure 2-1a with a single Gaussian applied and fit by the algorithm. The remaining unfitted signal (the residual) is shown below the fitted spectrum.

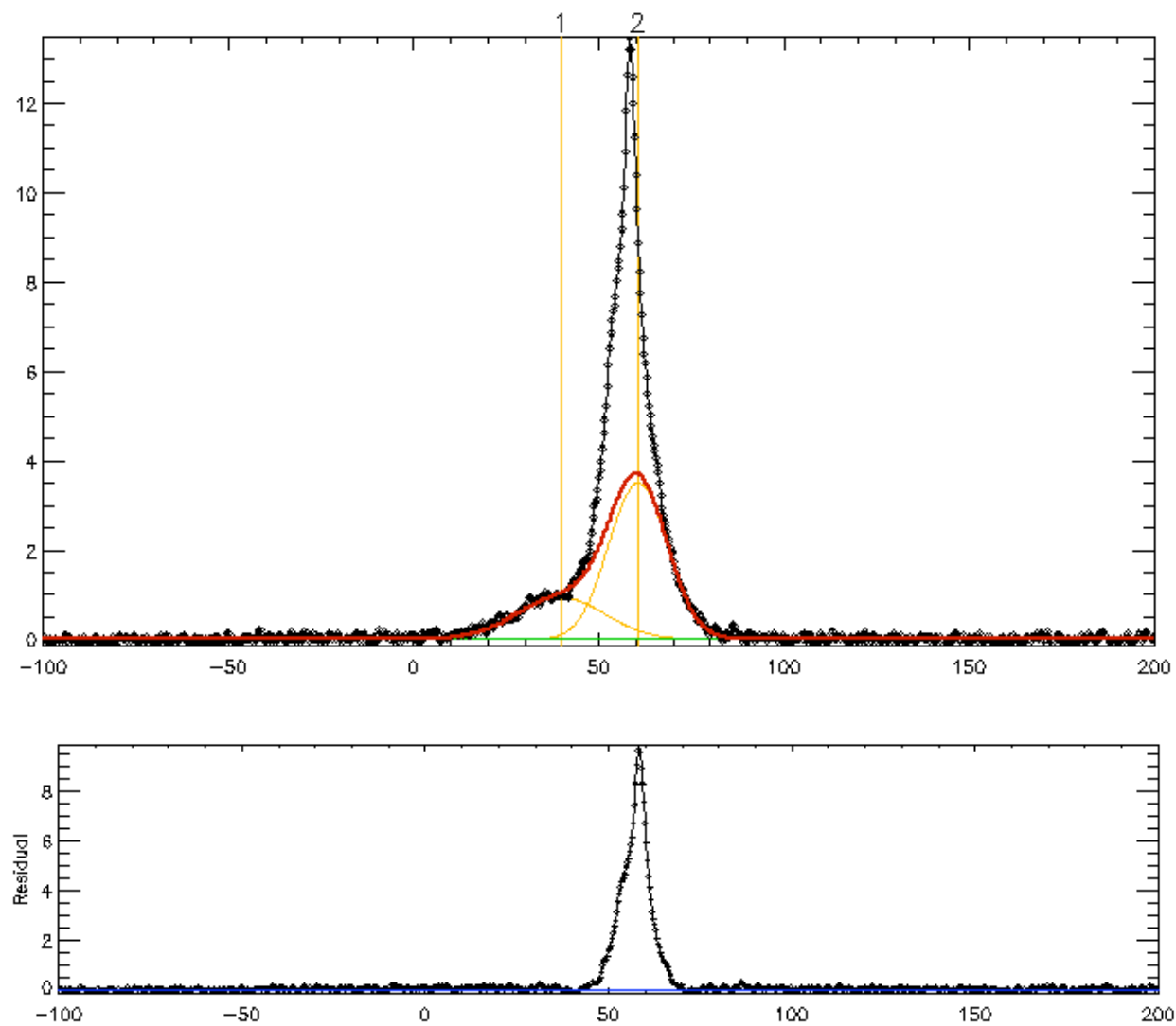


Figure 2-1 c. The same spectrum as in Figure 2-1a with two Gaussians applied.

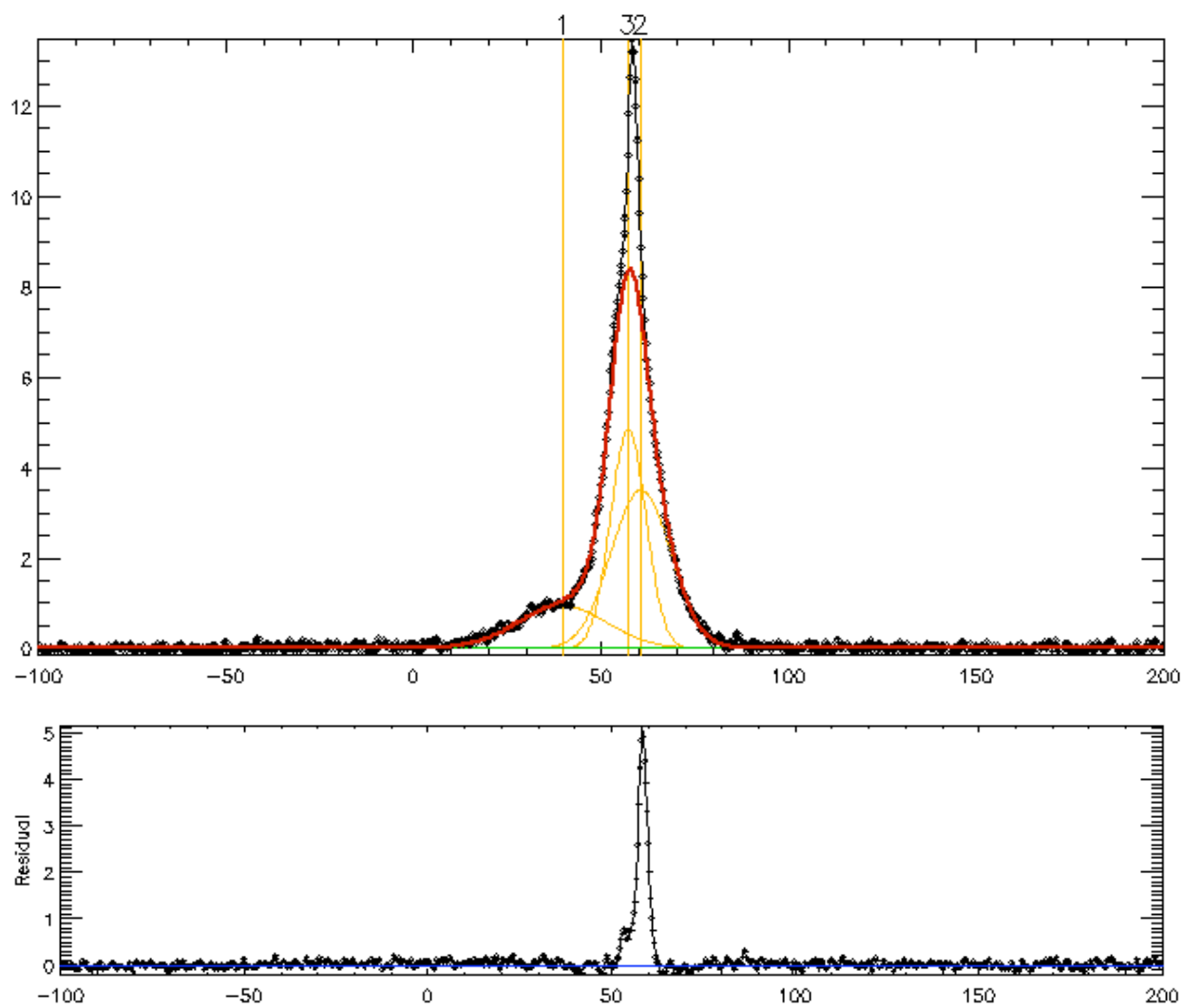


Figure 2-1 d. The same spectrum as Figure 2-1a with three Gaussians applied.

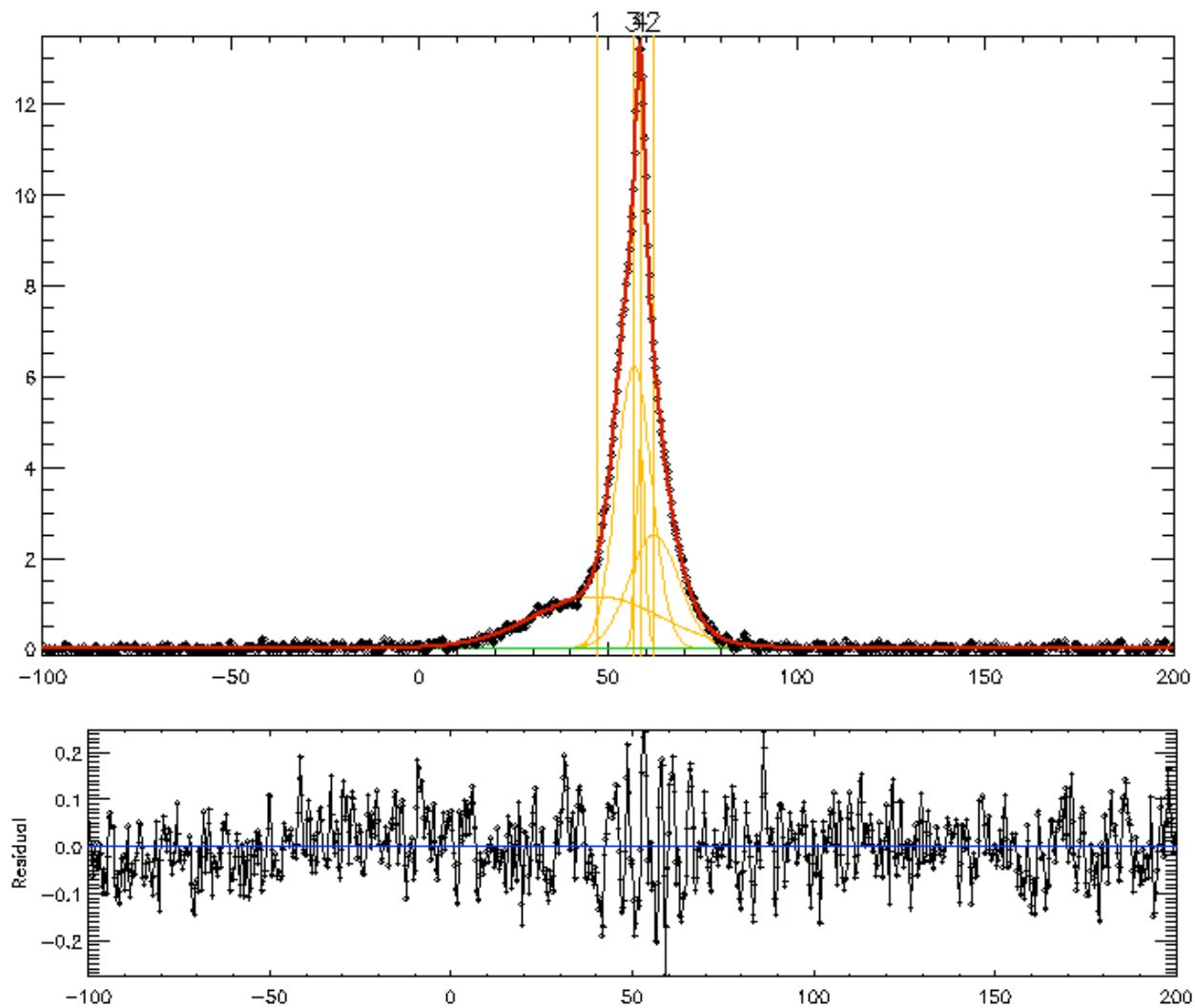


Figure 2-1 e. The fully fitted spectrum (4 Gaussians) to the profile in Figure 2-1a and its residual.

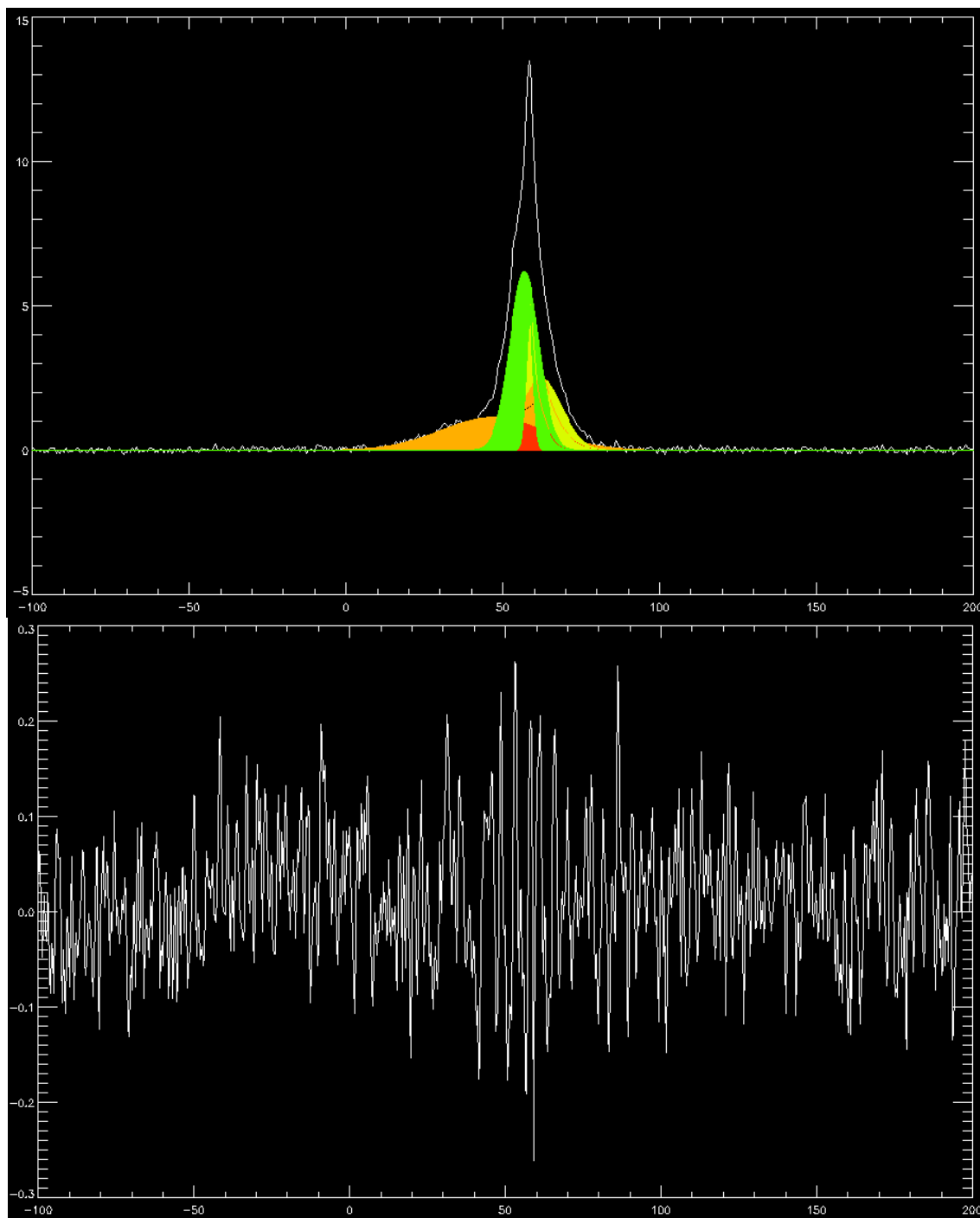


Figure 2-1 f. A color, graphic representation of the fitted spectrum presented to the fitter by the algorithm. See Section 2.2 for details.

exceptions, consistent results can be obtained. Perhaps more reassuringly, Haud and Kalberla (2007) have determined that fitting Gaussians to HI profiles by human judgement and by computer algorithms yield virtually the same results.

2.4 PREVIOUS WORK

This technique has been used several times before. Mebold (1972) decomposed about 1300 21-cm line profiles from the 25 meter Stockert radio observatory in Bad Münstereifel, Germany into approximately 2400 components. Mebold's work presented evidence in favor of a two-component interstellar HI gas; his profiles typically had one narrow, peaked ($s \approx 3$ km/s) and one broad, shallow ($s \approx 10$ km/s) component. The narrow components were observed in a limited region of the sky (about 50% of the observed positions). Due to the patchy distribution of the narrow components, Mebold interpreted the emission to be from HI concentrations or clouds. The shallow components were more smoothly distributed and observed at any position in the survey, and their intensity and radial velocity varied only slowly with position. He suggested that this component might be associated with a WNM at temperature ≈ 8000 K.

Mebold, Winnberg, Kalberla, and Goss (1982, hereafter MWKG) observed emission spectra towards 69 extragalactic radio sources using the MPIfR 100 m telescope near Bonn, Germany. MWKG found spin temperatures for the HI gas ranging from about 10 to about 3,000K. Most of the features were observed in the range of 20-140 K with a median of 86 K. MWKG also found evidence for warm (200-1,000 K) envelopes around cold HI cloud as well as hotter gas ($T \approx 10^5$ K) smoothly distributed between the clouds.

Verschuur and Schmeltz (1989) obtained emission profiles in 180 directions using the Arecibo Observatory and decomposed 172 profiles into approximately 800 components which

they plotted as a function of velocity. The bulk of their data showed a distinct peak at 3 km/s indicative of the CNM. However, unlike MWKG, their work did not show evidence for the existence of a WNM between 5,000–10,000 K.

Verschuur and Magnani (1994) used data from three facilities (the Arecibo 304 meter, NRAO 140 ft, and the Hat Creek 25 meter) to decompose over 1100 profiles into over 4000 components. Their work presented evidence in favor of the CNM, the WNM, and a third, unidentified component. The components were given numerical designations. “Component 3” has typical linewidths of 3 km/s matching Mebold’s “narrow” component and is clearly associated with the CNM. “Component 2” has typical linewidths of 12 km/s, close to Mebold’s estimate of ≈ 10 km/s and is likely associated with the WNM. The component that Verschuur and Magnani detected that had not been previously seen, or at least, identified explicitly, was dubbed “Component 1”, a very wide component ($\sigma \approx 25$ -50 km/s) that could not be interpreted in terms of temperature (25 km/s would be equivalent to 25,000 K). Verschuur and Magnani speculated that this broad component might not arise from the ISM but might be associated with stray radiation in the sidelobes of the telescope. Verschuur and Peratt (1996) analyzed HI data that had been corrected for stray radiation and determined that the broad component was real, though they subdivided this component into 2 distinct velocity regimes (≈ 31 km/s and ≈ 50 km/s).

Most recently, Haud and Kalberla (2007) used a computer algorithm to deconvolve HI profiles from the Leiden/Argentine/Bonn (LAB) all-sky survey of Galactic HI (nearly 190,000 spectra). They find 4 groupings of widths: 3.9 ± 0.6 km/s, 11.8 ± 0.5 km/s, 24.1 ± 0.6 km/s, and 42 ± 5 km/s. The authors conclude that the 3.9 and 24.1 km/s groups are the thermally stable

CNM and WNM phases discussed in Chapter 1. The 11.8 km/s grouping is a warm, thermally unstable phase, and the reality and origin of the 42 km/s grouping are “obscure”.

The observations presented in this thesis are from the GBT, NRAO’s Green Bank Telescope in West Virginia, which was built to minimize side lobe contamination of HI signals. One of the principal aims of this thesis is to determine whether the very broad component identified by Verschuur and Magnani (1994), Verschuur and Peratt (1996), and Haud and Kalberla (2007) is “real” or not. Our observations are described in the following Chapter.

CHAPTER 3

THE OBSERVATIONS

3.1 THE HI DRIFT SCAN SURVEY

The 21 cm observations were made with the 100 m Green Bank Telescope (GBT) in Green Bank, WV during June, 2003 while the telescope was immobilized during the day because of repairs to the circular track. The data were taken as part of a drift scan survey toward the center of the local supercluster including the Virgo cluster and its foreground to study strategies for large scale HI extragalactic redshift surveys (Haynes, et al. 2003). Our portion of the data was confined to the local HI Galactic emission and covers the 5 MHz centered on the 1420 MHz line. The total bandwidth of the observations was 50 MHz with the remaining 45 MHz covering the redshifted HI line. The velocity resolution of the observations was 1.526 kHz equivalent to 0.32 km/s. Spectra were obtained in drift scan mode dumping the data every 10 s for a spatial resolution of 2.5'. The beam of the telescope at 1420 MHz is 9' so the data are oversampled but were combined along R.A. by adding 4 adjacent scans together to give 10' angular resolution in that coordinate. Combining the data in this fashion resulted in a total of 5,787 spectra. Of these 526 were not useable because the velocity scale for these scans was not set to be the velocity of the local standard of rest, but rather, the heliocentric velocity. Because we have more than enough scans using the correct velocity scale for our purposes, we did not deem it necessary to convert the 526 scans to LSR velocity.

Eleven strips at declinations varying by 4' were taken over a period of 12 days. The declination coverage was $15^{\circ} 0.4'$ to $15^{\circ} 40'$. The sky distribution of the observed strips is shown in Figure 3-1 (the angular scale of observations is slightly exaggerated for clarity). Figure 3-2 shows sample spectra from our data set. The typical rms of a single spectrum (i.e., when 4 scans are added in R.A.) is 0.06-0.08 K. This is significantly better than most HI surveys.

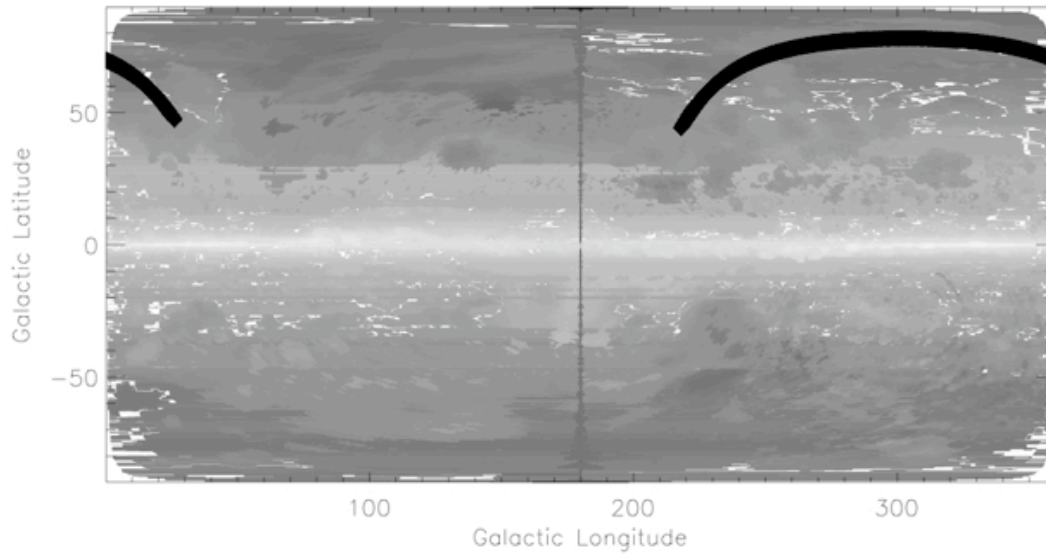


Figure 3-1. Sky distribution of the 21 cm drift scan observations used in this thesis (the thick black line in the northern Galactic hemisphere) superposed on a map of the HI column density (e.g., Dickey and Lockman 1990).

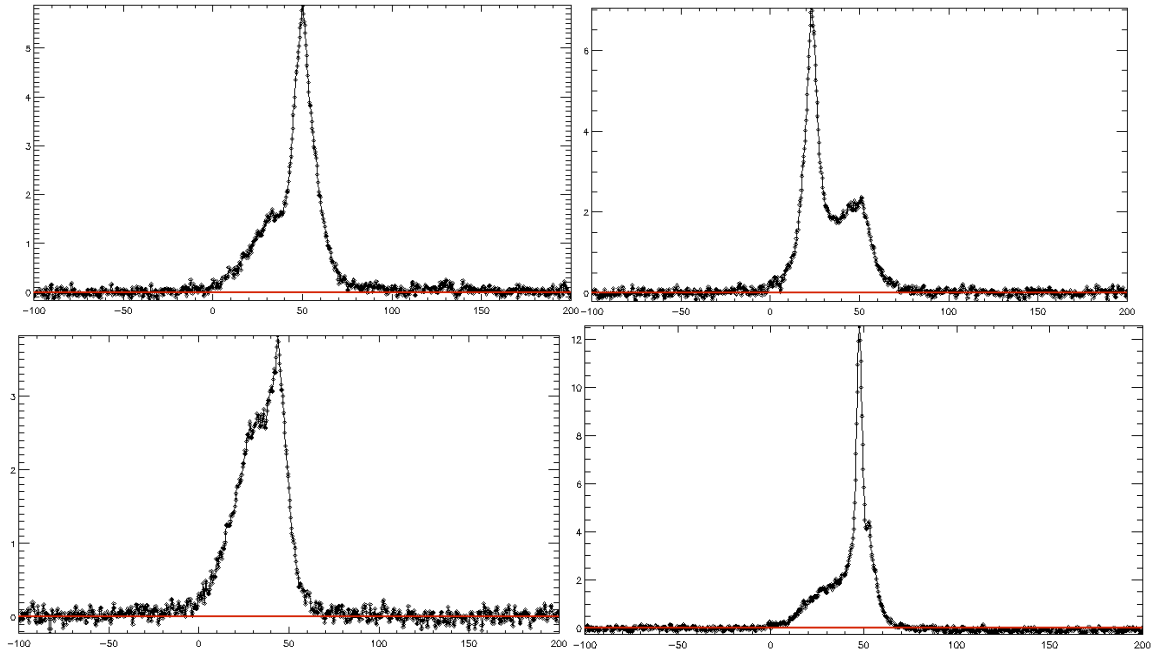


Figure 3-2a. Sample spectra from the data set. These spectra were obtained by adding 4 scans adjacent in R.A. The horizontal scale is LSR velocity in km/s and the y axis is antenna temperature in K.

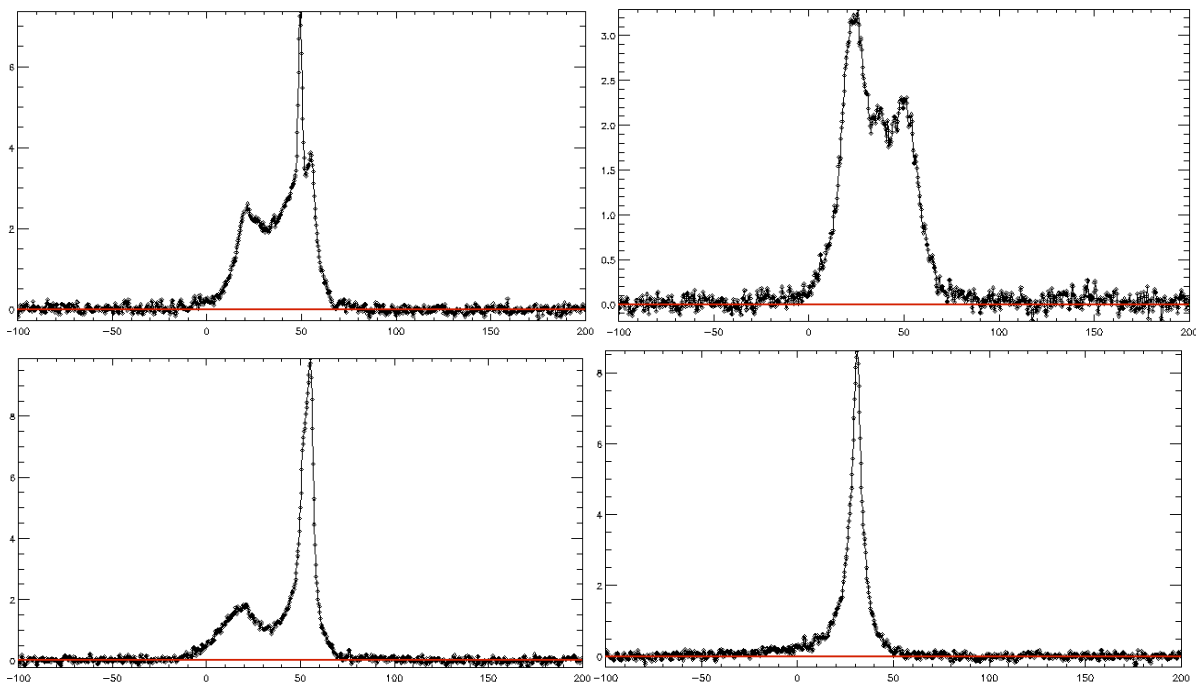


Figure 3-2b. Same as 3-2a.

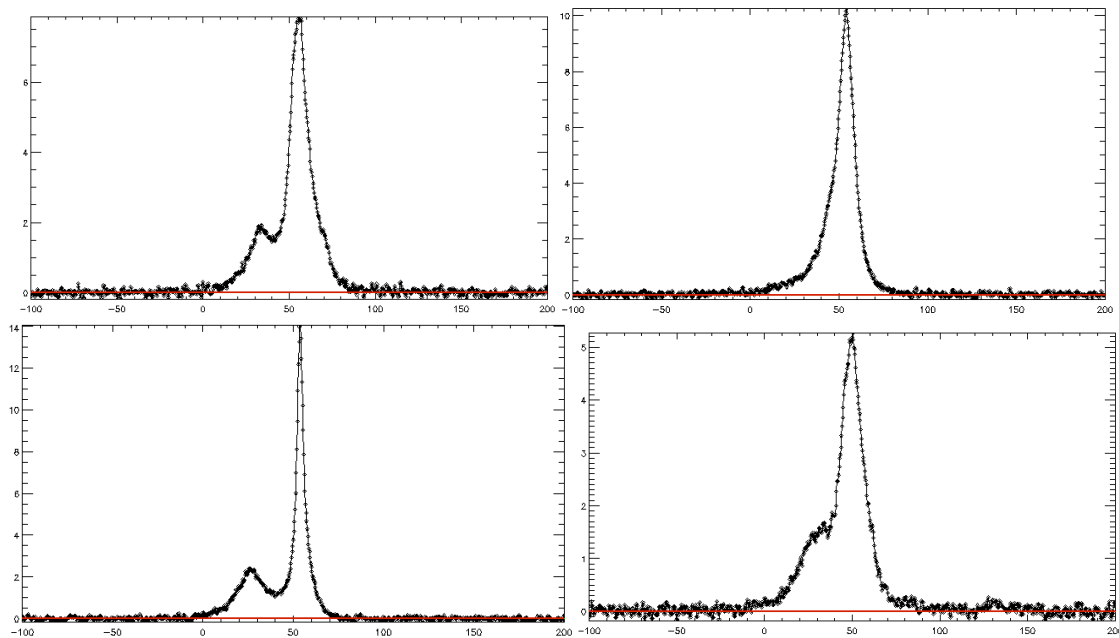


Figure 3-2c. Same as 3-2a.

3.2 HIGH VELOCITY CLOUDS

During the analysis of the survey data, we serendipitously found 137 spectra with clear evidence of high-velocity HI clouds in addition to the typical low-velocity profile. High-velocity clouds exhibit velocities substantially greater than what the Milky Way's typical rotation curve predicts at any given position. By definition, high velocity clouds have a local standard rest velocity, $|v_{\text{lsr}}| \geq 90$ km/s (see Wakker 1991). Figure 3-3 shows a few examples of these high-velocity clouds in our sample. Table 3-1 lists the positions and velocities of these objects, which are not analyzed any further in this thesis.

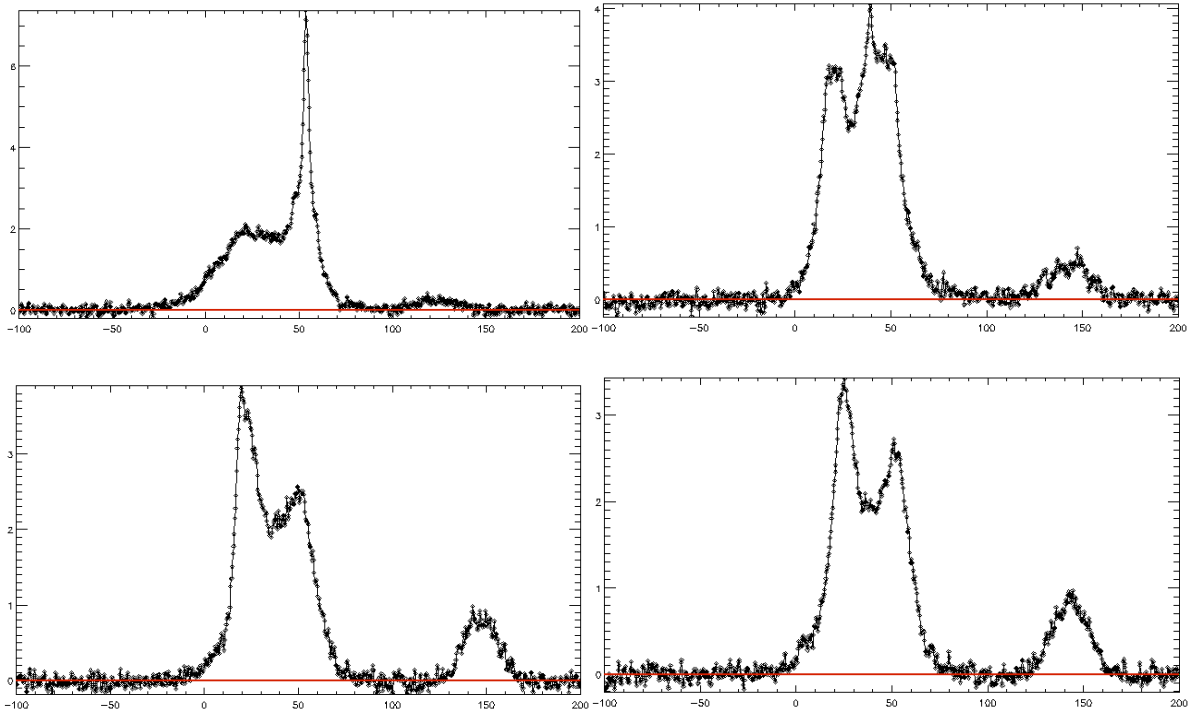


Figure 3-3. A few examples of high velocity clouds that were found in the data. High-velocity clouds are defined as HI features with $|v_{\text{lsr}}| \geq 90$ km/s. The axes are as in Figure 3-2.

Table 3-1. List of the high velocity clouds detected in the data. Center velocities marked with an asterisk denote scans where the velocity scale was not set to the local standard of rest. These latter objects were identified as high-velocity clouds by inspection.

Right Ascension (2000.0) degrees	Declination (2000.0) degrees	Center Velocity (km/s)	Peak Antenna Temperature (K)
163.313	15.006	130	0.2
163.480	15.006	125	0.1
164.024	15.006	100	0.15
164.694	15.006	100	0.15
168.041	15.007	100	0.15
170.886	15.007	125	0.15
171.053	15.007	125	0.25
171.220	15.007	120	0.2
182.270	15.007	150	0.2
182.437	15.007	150	0.2
182.605	15.007	150	0.2
182.772	15.007	155	0.35
182.939	15.007	150	0.3
183.107	15.007	145	0.55
183.274	15.007	145	0.5
156.066	15.069	94	0.25
161.957	15.069	125	0.2
170.994	15.070	124	0.23
171.161	15.070	122	0.2
171.831	15.070	115	0.3
182.236	15.071	150	0.37
182.403	15.071	150	0.2
182.738	15.071	160	0.17

182.905	15.071	145	0.24
183.073	15.071	144	0.47
183.240	15.071	143	0.35
163.427	15.136	131	0.15
164.598	15.137	100	0.21
164.765	15.137	100	0.15
164.933	15.136	100	0.15
170.957	15.137	125	0.22
171.124	15.137	125	0.22
171.794	15.137	115	0.26
171.961	15.138	115	0.23
181.827	15.138	146	0.17
181.994	15.137	148	0.18
182.162	15.138	150	0.17
182.329	15.138	148	0.21
182.988	15.137	142	0.28
183.165	15.137	144	0.31
170.993	15.204	125	0.24
171.160	15.206	123	0.18
171.830	15.204	115	0.32
171.997	15.204	115	0.21
181.745	15.204	147	0.31
181.913	15.204	148	0.49
182.080	15.204	148	0.25
182.248	15.204	151	0.22
182.917	15.204	142	0.24
183.084	15.204	148	0.17
171.185	15.271	125	0.18

171.352	15.271	125	0.20
171.687	15.271	112	0.18
171.854	15.271	114	0.26
172.021	15.271	113	0.19
181.590	15.272	146	0.14
181.757	15.272	147	0.53
181.925	15.272	147	0.86
182.092	15.272	147	0.58
182.259	15.272	150	0.33
182.929	15.272	143	0.27
183.096	15.272	148	0.18
161.882	15.402	120	0.21
162.049	15.402	88	0.20
171.062	15.402	125	0.17
171.229	15.403	124	0.21
171.397	15.403	121	0.26
171.564	15.403	118	0.12
172.233	15.403	114	0.18
181.647	15.404	144	0.43
181.773	15.404	145	0.78
181.940	15.404	144	0.91
182.107	15.404	144	0.61
182.275	15.404	146	0.39
182.994	15.404	147	0.21
183.111	15.404	150	0.22
183.279	15.404	156	0.14
165.383	15.463	120	0.21
175.666	15.463	125	0.16

175.833	15.463	124	0.21
176.001	15.463	121	0.27
176.670	15.463	114	0.18
176.838	15.463	114	0.20
181.523	15.463	144	0.24
181.691	15.463	143	0.65
181.858	15.463	143	0.86
182.026	15.464	142	0.63
182.193	15.463	144	0.31
182.360	15.463	148	0.15
182.862	15.463	157	0.14
183.030	15.463	149	0.25
183.197	15.463	152	0.19
150.223	15.535	117	0.14
150.391	15.534	117	0.14
150.558	15.534	114	0.13
161.938	15.534	122	0.18
163.110	15.536	146	0.14
163.444	15.536	131	0.13
163.611	15.536	215	0.19
163.779	15.535	216	0.23
163.946	15.536	212	0.13
171.356	15.537	118	0.24
171.523	15.537	117	0.16
181.607	15.538	143	0.35
181.775	15.538	142	0.59
181.942	15.538	140	0.56
182.109	15.538	143	0.19

182.946	15.538	152	0.20
183.113	15.538	152	0.17
195.575	15.537	95	0.15
163.186	15.600	*	0.18
163.687	15.599	*	0.21
163.854	15.600	*	0.21
171.385	15.600	*	0.19
172.220	15.600	*	0.26
181.566	15.600	*	0.16
181.691	15.600	*	0.30
182.677	15.600	*	0.16
182.844	15.600	*	0.15
183.010	15.600	*	0.19
183.344	15.600	*	0.14
184.634	15.600	*	0.14
163.154	15.667	*	0.20
163.674	15.667	*	0.19
163.847	15.667	*	0.21
172.128	15.667	*	0.25
172.301	15.667	*	0.27
175.474	15.667	*	0.18
175.074	15.667	*	0.14
175.421	15.667	*	0.14
175.594	15.667	*	0.19
175.768	15.667	*	0.15
182.748	15.667	110	0.16
183.094	15.667	108	0.17
183.238	15.667	120	0.19

184.308	15.667	124	0.14
162 3.84	15 32.12	114	0.14

CHAPTER 4

RESULTS

In Chapter 2 we discussed the mechanisms that broaden spectral lines: natural, collisional, and Doppler broadening. In the case of interstellar atomic hydrogen, Doppler broadening dominates by many orders of magnitude and we can assume the spectral profiles in Chapter 3 are broadened by the motion of the hydrogen atoms along the line of sight (Spitzer 1978) resulting in Gaussian line shapes. For the moment, we will assume that a single Gaussian-fit component arises from the same distinct region along the line of sight (we will revisit this in Chapter 5) so that the width of the Gaussian component reflects the thermal motion of the gas in that region.

In this case, the velocity dispersion, σ_v , of the line ($2.35\sigma_v = \text{FWHM}$) can be converted to a temperature using the equipartition energy relation

$$1/2(m_H\sigma_v^2) = 3/2(kT)$$

where m_H is the mass of hydrogen and k is Boltzmann's constant. Plugging in the constants and solving for T yields

$$T = 40 \sigma_v^2 \text{ K}$$

where σ_v is measured in km/s. With this formalism, we can produce histograms of the number of components vs. velocity dispersion and also the area of the components (which is proportional to $N(\text{HI})$) vs. velocity dispersion. These histograms for the 11 strips of data are presented in Figure 4-1. In Figure 4-2, we present the histograms for all the data added together. We will use this latter figure for our analysis.

In Figure 4-2, the distribution of the area of the components as a function of the velocity dispersion shows clearly visible features at $\approx 3\text{-}4$ km/s, $\approx 10\text{-}17$ km/s, and ≈ 40 km/s. These features have typical velocities that correspond to temperatures of $\approx 360\text{-}640$ K, $4,000\text{-}11,000$ K, and $64,000$ K, respectively. This is the principal result of this thesis and the physical implications of these groupings of linewidths are discussed in Chapter 5.

The histograms of the number of components vs. velocity dispersion show the group peak at $3\text{-}4$ km/s and 40 km/s, though the peak at $10\text{-}17$ km/s is indistinct. The histogram of the areas of the components vs. velocity dispersion is more relevant because the area of a Gaussian profile is proportional to $N(\text{HI})$ via the equation valid for optically thin gas:

$$N(\text{HI}) = 1.823 \times 10^{18} \int T_B dv \text{ cm}^{-2}$$

Where $\int T_B dv$ is the area of the line profiles. Thus, our results (i.e., 3 distinct components in the area histogram) fully support what had been seen by Verschuur and Magnani (1994), Verschuur and Peratt (1999), and Haud and Kalberla (2007). The latter authors found four components with 3.9 ± 0.6 km/s, 11.8 ± 0.5 km/s, 24.1 ± 0.6 km/s, and 42 ± 5 km/s based on an algorithm driven fitting of nearly 190,000 spectra covering the entire sky. Although we see 3 of these components, we do not see evidence for the 24.1 ± 0.6 km/s grouping in our data. Our data differs from the Haud and Kalberla data in that we sample a relatively small sample of the sky and all of it at high Galactic latitudes, our resolution is better in velocity (0.32 vs. $1.03\text{-}1.27$ km/s) and spatially ($9'$ vs. $30'\text{-}36'$), and most importantly, our data were taken with the Green Bank Telescope whose off-axis feed design minimizing stray radiation and interference is better than any other telescope at this wavelength. (see <https://wikio.nrao.edu/bin/view/GBT/GBTSensitivityComparison>). Thus, we can state with confidence what no one has explicitly stated before: the broadest component with a width of ≈ 40

km/s is a real feature of the ISM and is almost surely not instrumental. We will discuss the implications of our finding in the next Chapter.

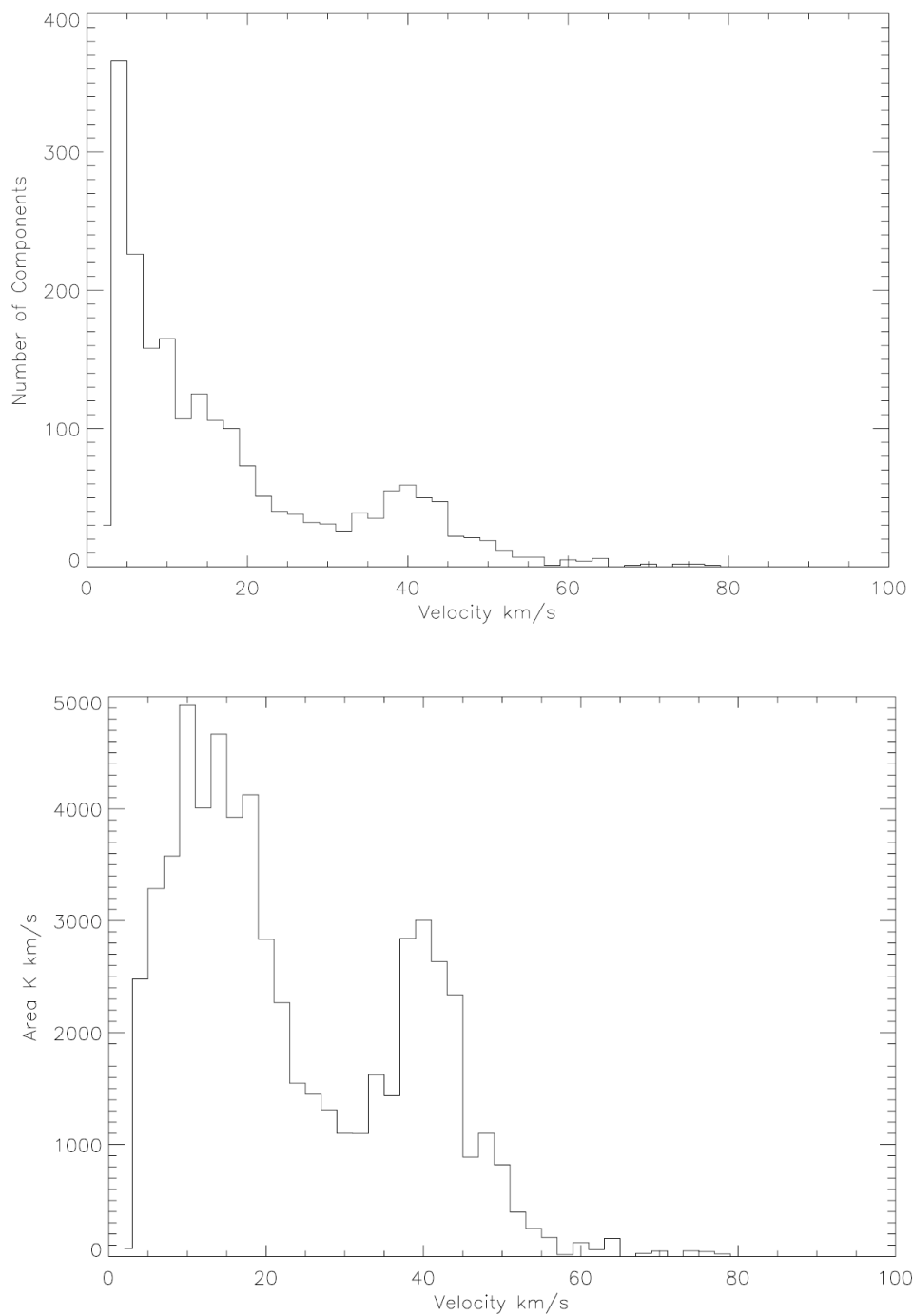


Figure 4-1a. (Top) Histograms of the data plotted as number of components vs. velocity dispersion for Strip 1. (Bottom) The area of the Gaussian fit components vs. velocity dispersion for Strip 1.

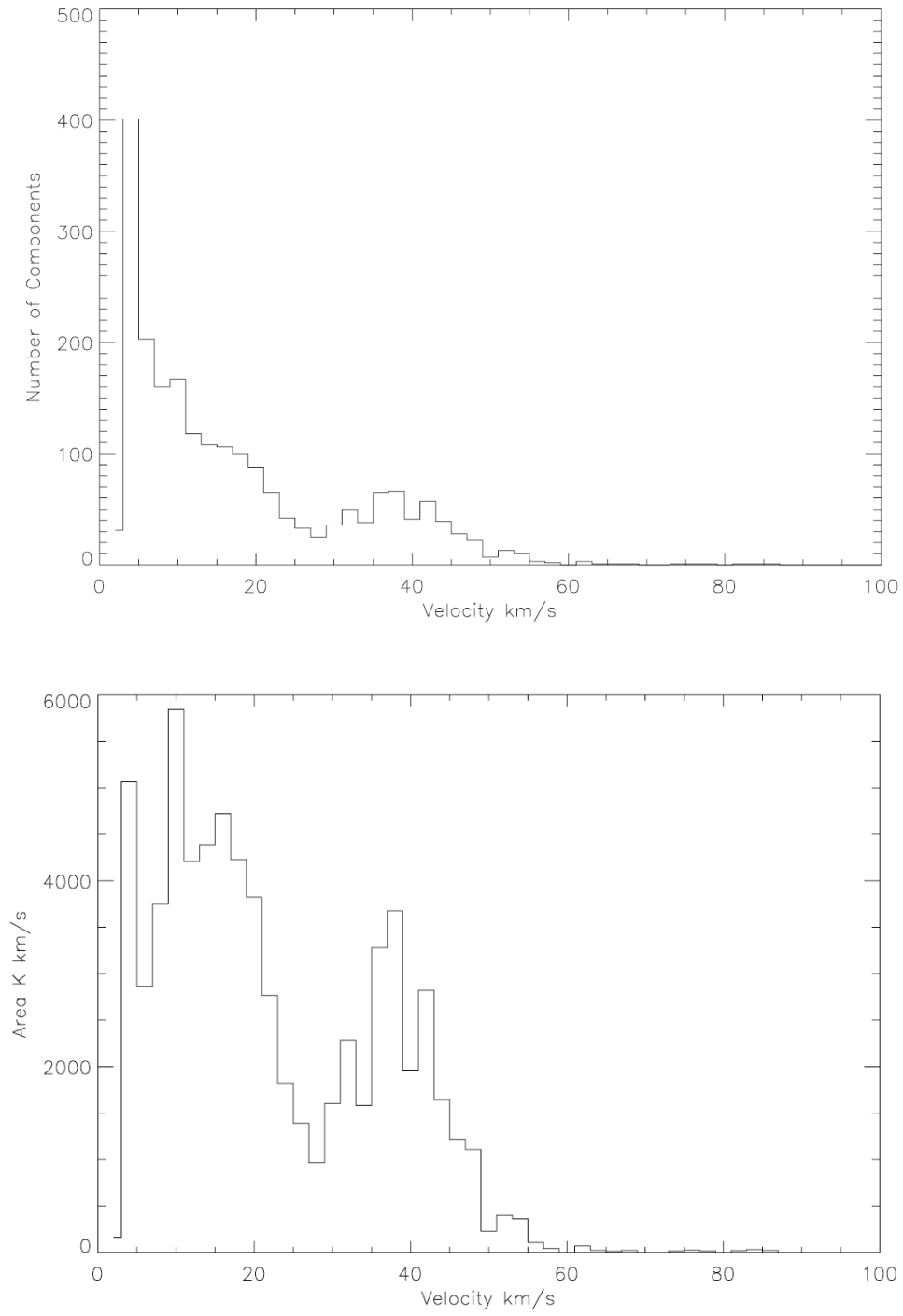


Figure 4-1b. Same as 4-1a for Strip 2.

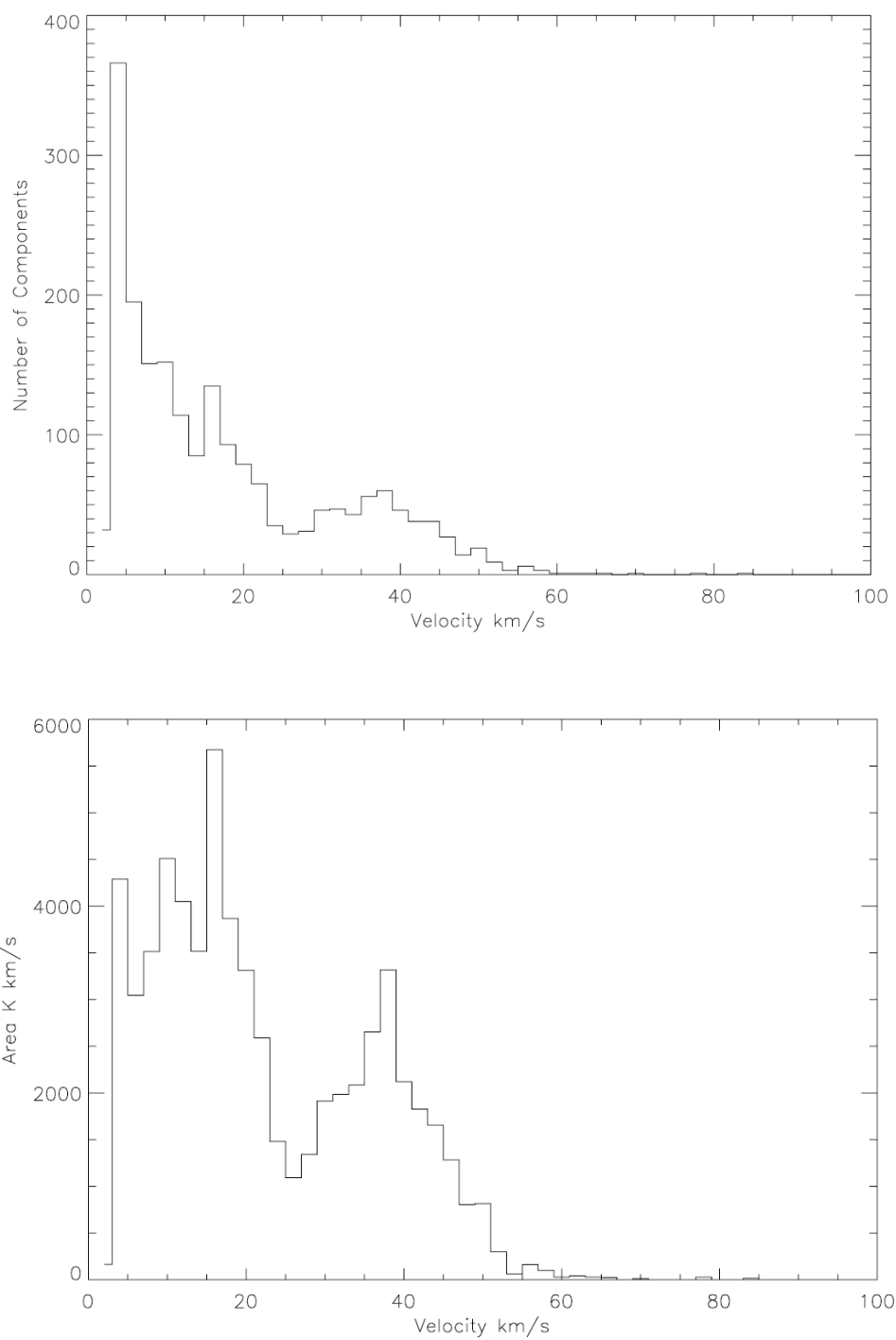


Figure 4-1c. Same as 4-1a for Strip 3.

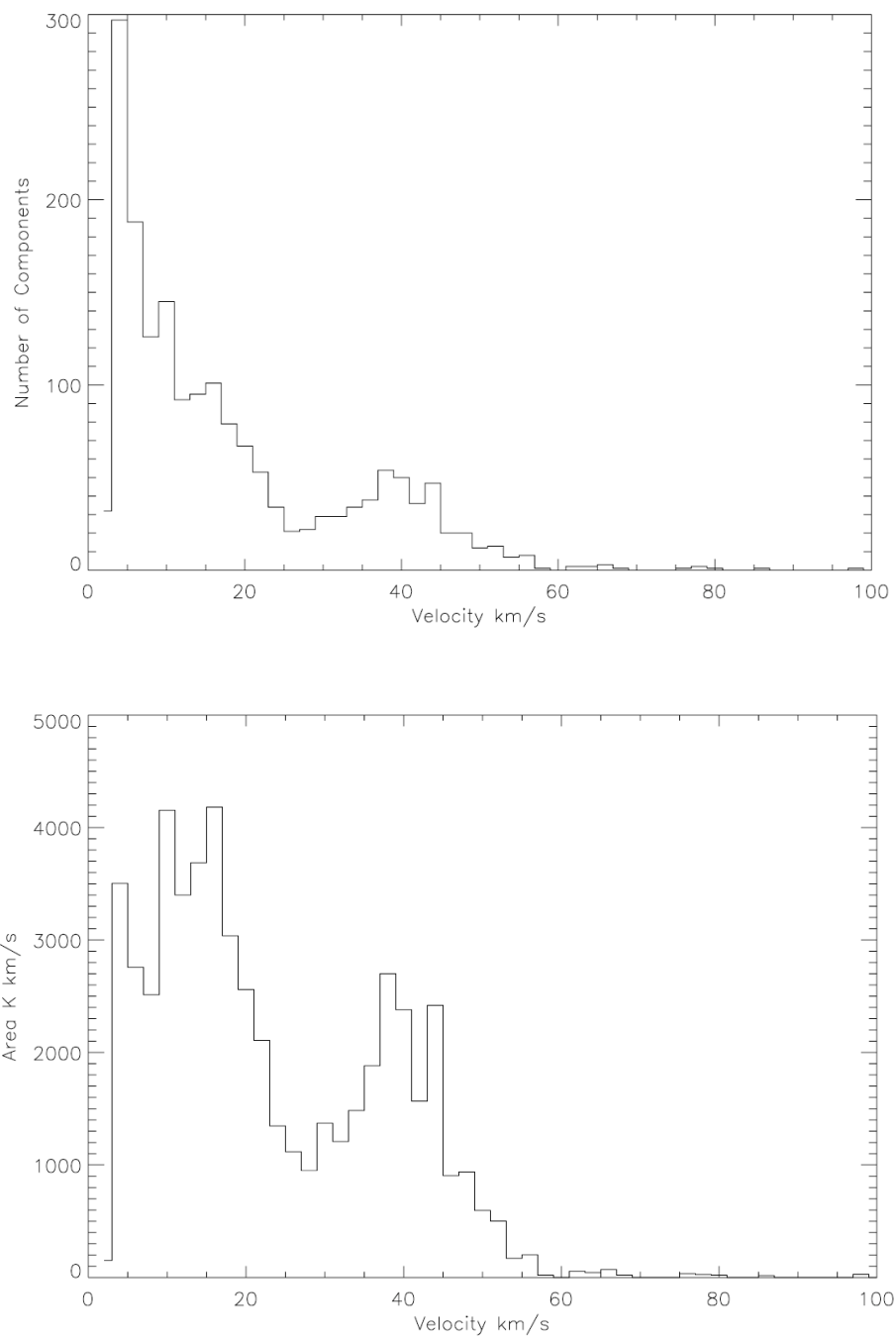


Figure 4-1d. Same as 4-1a for Strip 4.

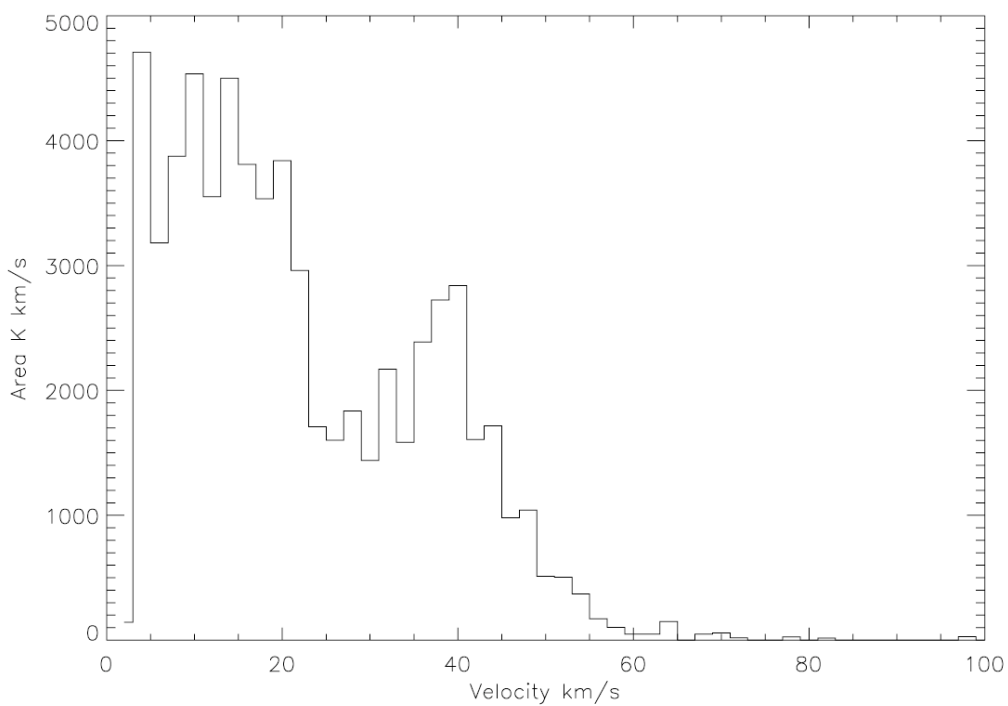
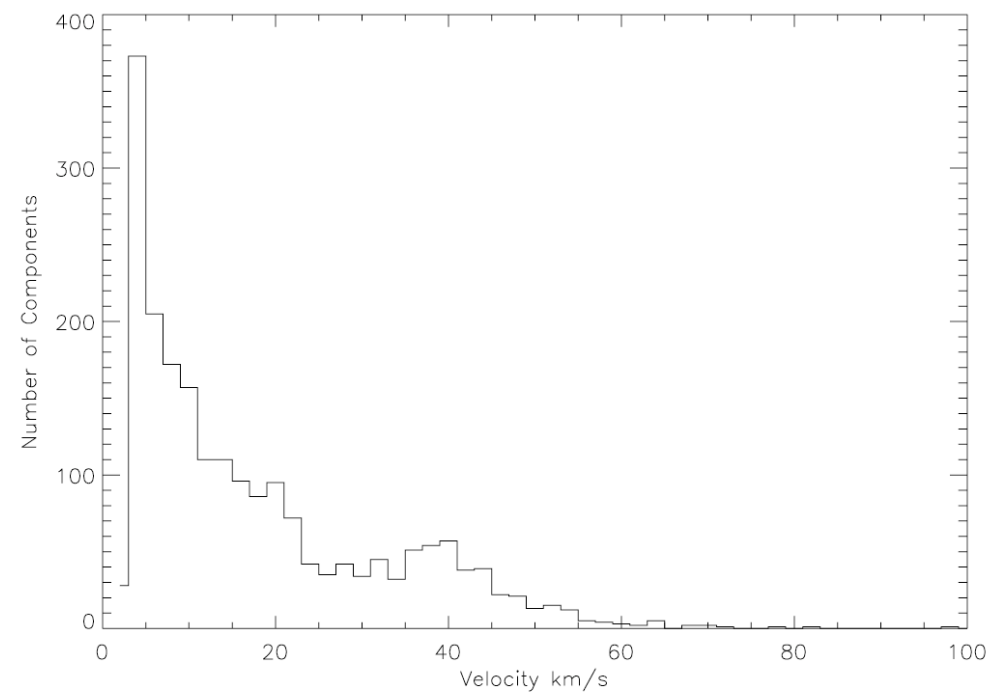


Figure 4-1e. Same as 4-1a for Strip 5.

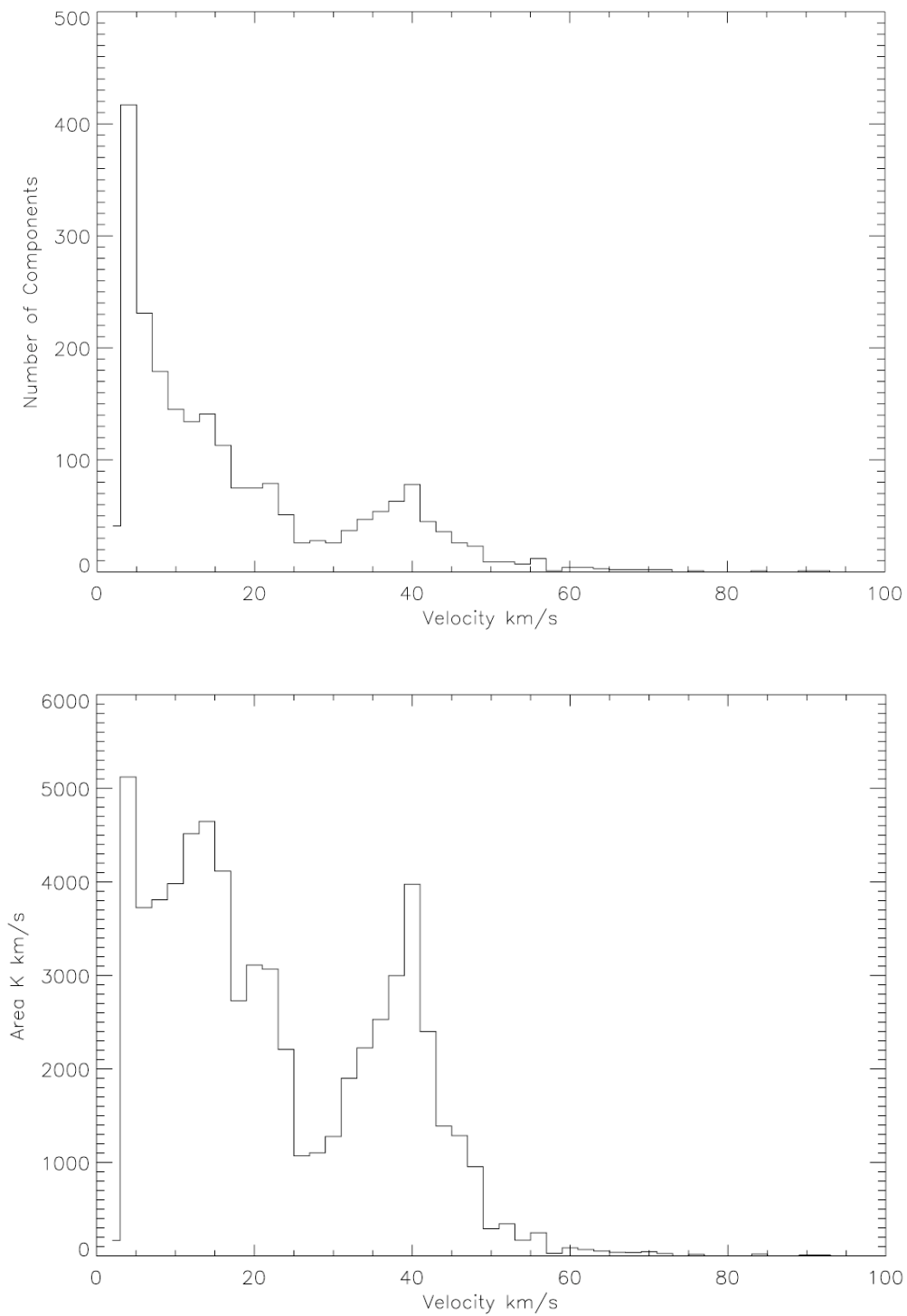


Figure 4-1f. Same as 4-1a for Strip 7.

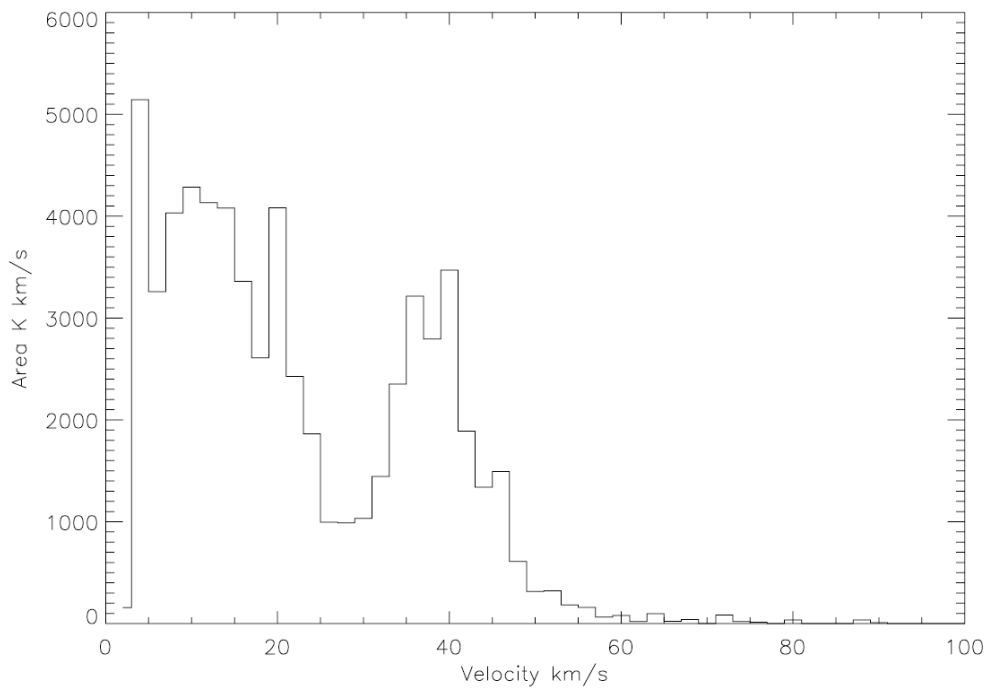
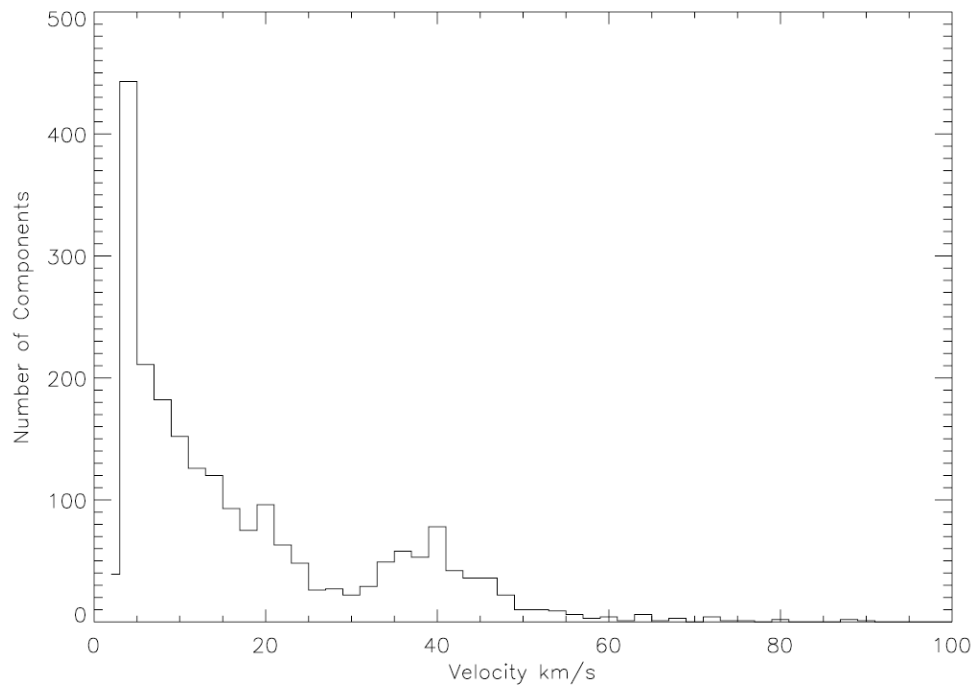


Figure 4-1g. Same as 4-1a for Strip 8

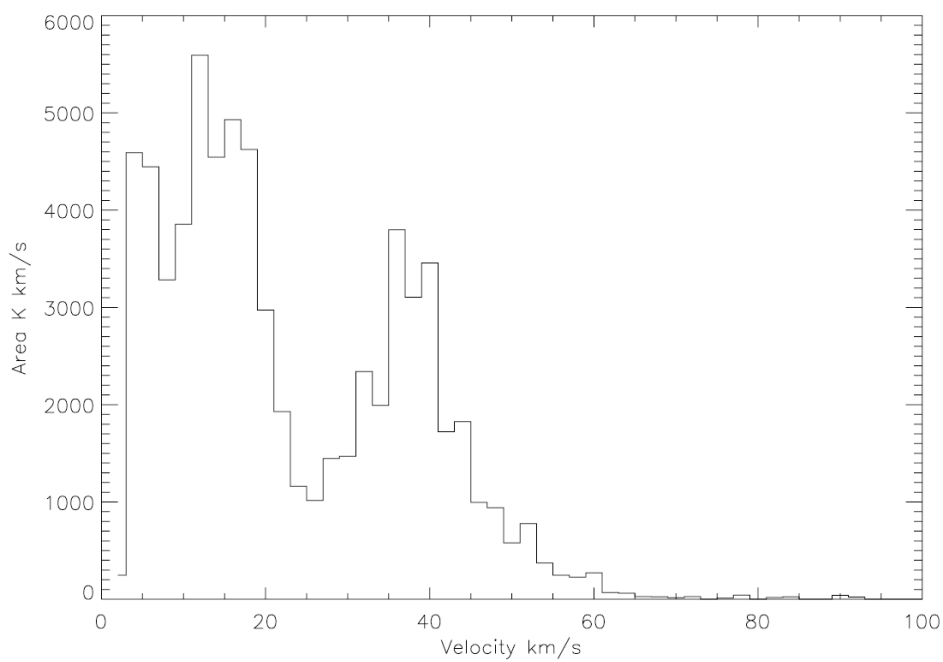
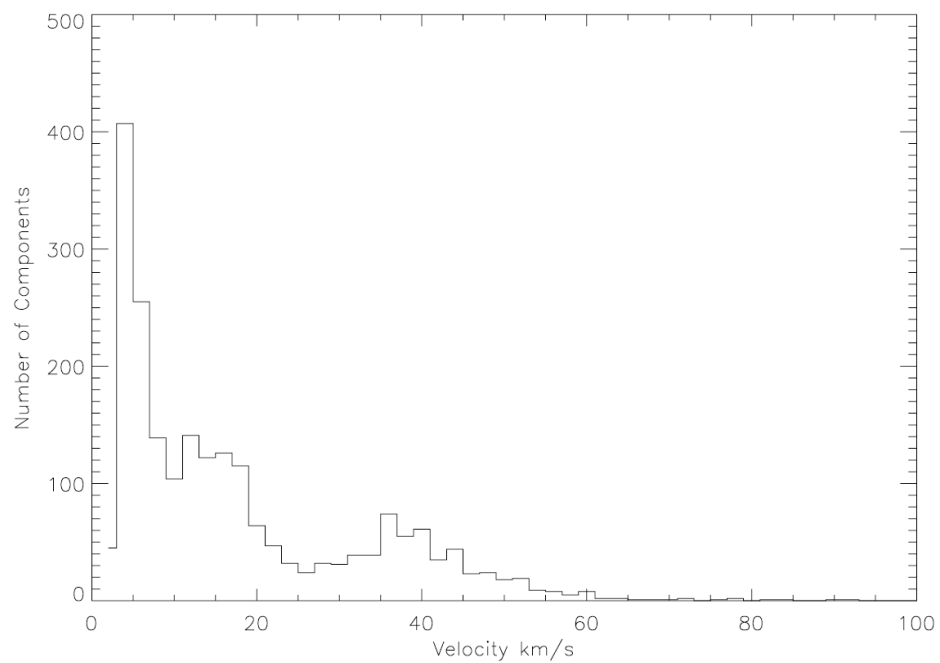


Figure 4-1h. Same as 4-1a for Strip 9.

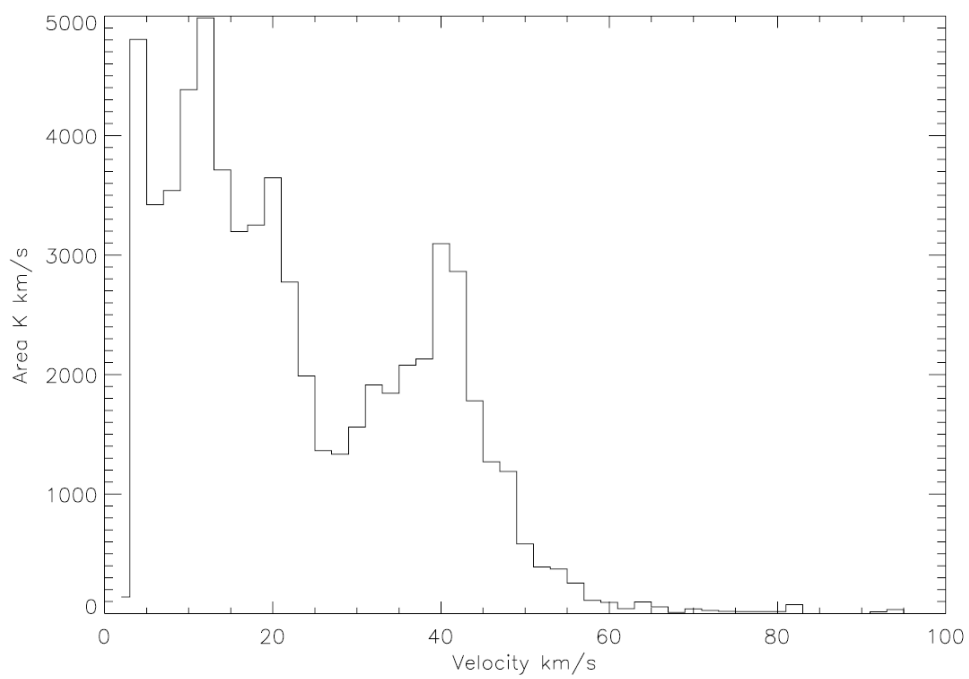
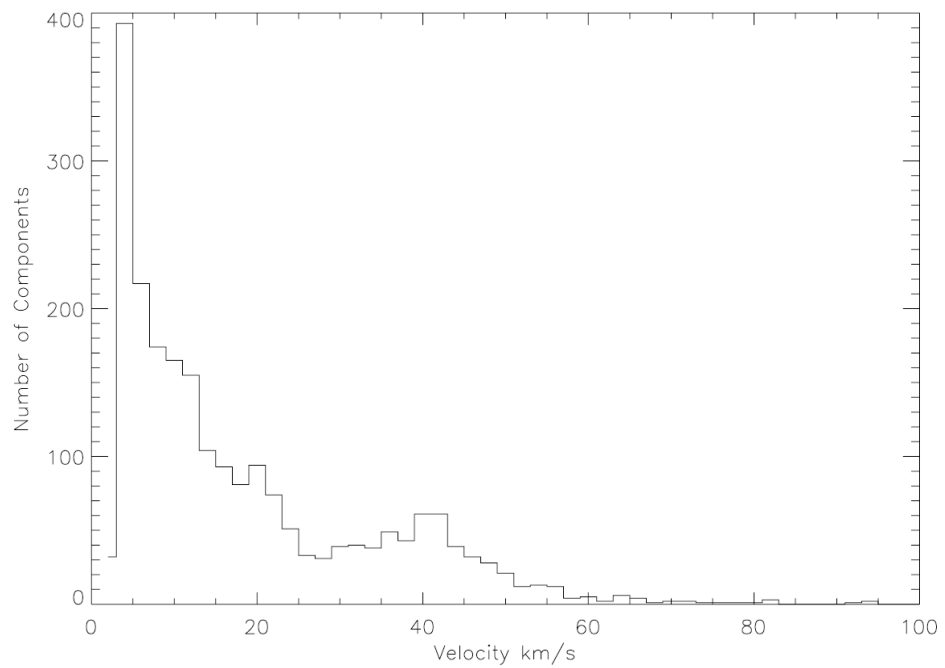


Figure 4-1i. Same as 4-1a for Strip 10.

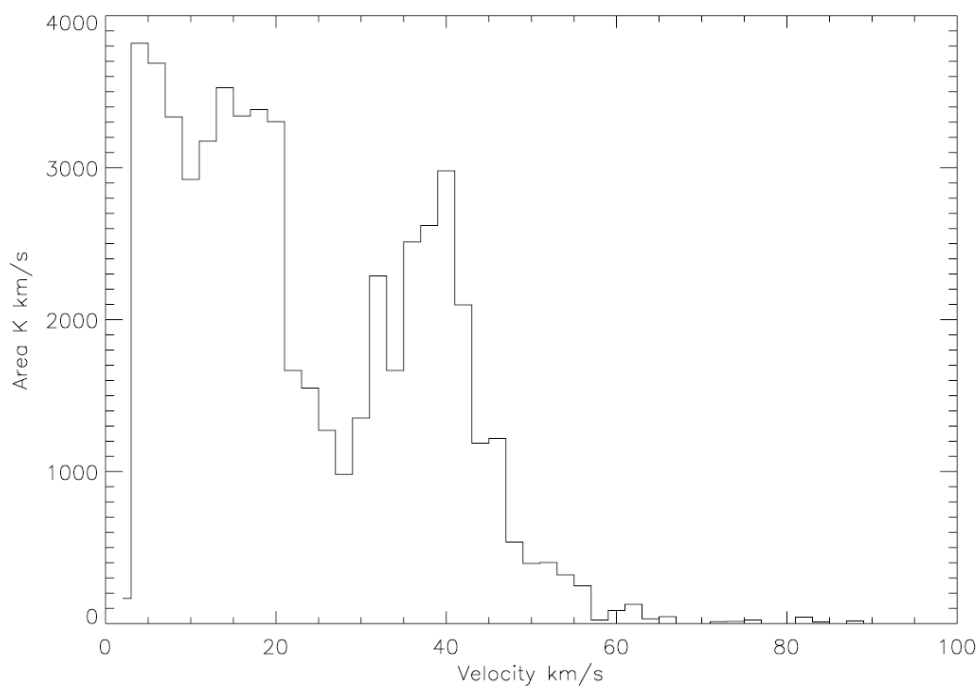
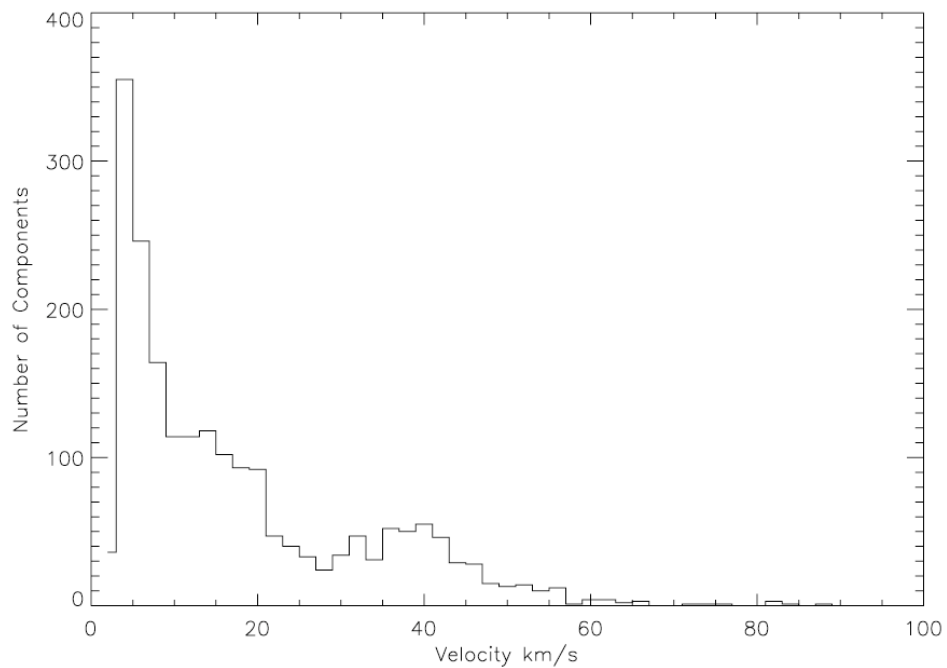


Figure 4-1j. Same as 4-1a for Strip 11.

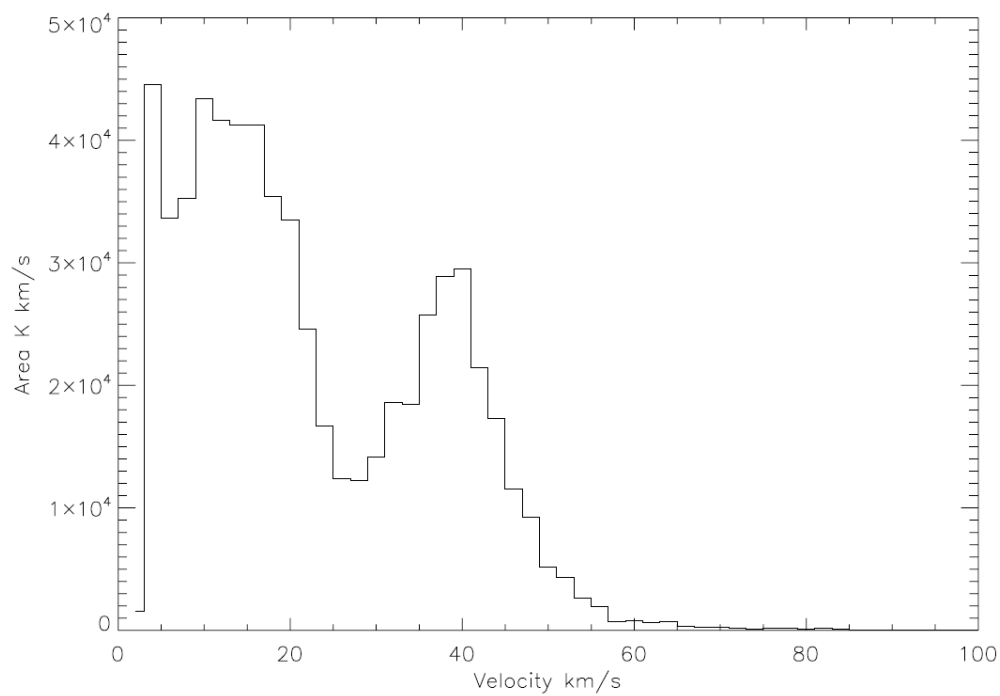
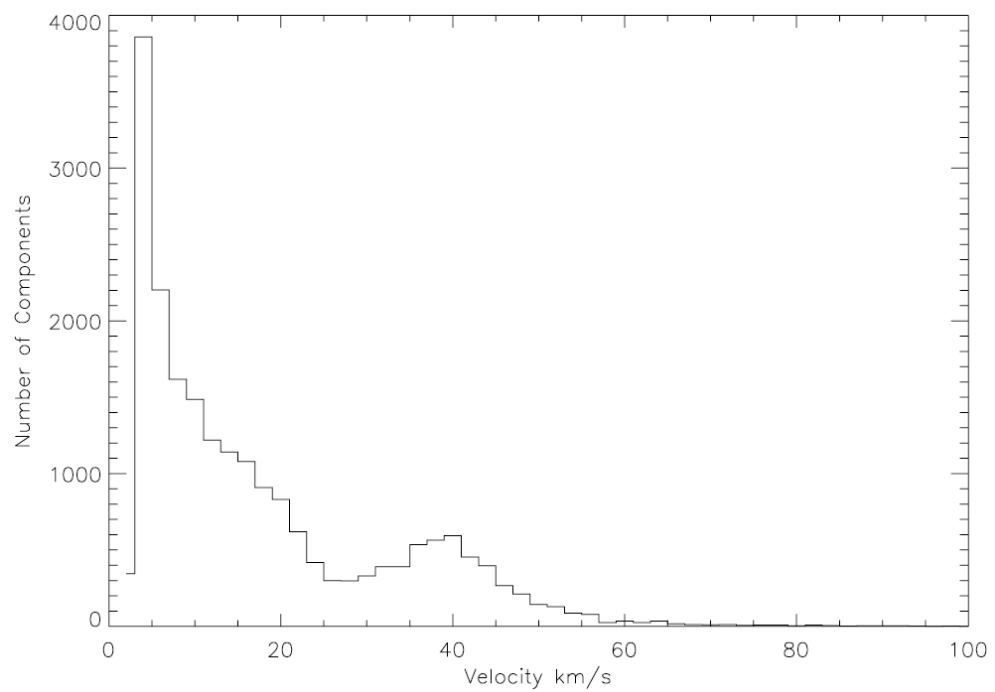


Figure 4-2. Same as 4-1a for all of the Strips.

CHAPTER 5

DISCUSSION

As we saw in Chapter 4, our data shows evidence for 3 distinct features at $\approx 3\text{-}4$ km/s, $\approx 10\text{-}17$ km/s, and ≈ 40 km/s corresponding to temperatures of $\approx 360\text{-}640$ K, $4,000\text{-}11,000$ K, and $64,000$ K, respectively. The $360\text{-}640$ K component can be identified with the CNM. The component is warmer than expected, but that is likely due to contributions of several clouds along the line of sight. Spitzer talks about a “standard cloud” in the ISM, a typical HI cloud with $N(\text{HI}) \approx 4 \times 10^{20} \text{ cm}^{-2}$, $n = 20 \text{ cm}^{-3}$, $T = 80 \text{ K}$, $\tau_v = 0.2$, and size ≈ 6 pc. He calculates in Spitzer (1978) that there are 6.2 clouds per kpc.

Our sightlines are at least a few hundred pc in length, and likely longer, before the halo is reached so it is likely there are several CNM clouds along any line of sight. In this case the CNM contribution to a spectral feature is

$$\sigma_v^2(\text{CNM}) = n\sigma_v^2(\text{standard cloud})$$

where $\sigma_v(\text{standard cloud}) = 1.6$ km/s and n is the number of clouds along a line of sight.

Conservatively choosing $n = 3\text{-}4$, $\sigma_v(\text{CNM})$ yields $2.8\text{-}3.2$ km/s, very similar to our observed value.

The feature corresponding to a temperature of $4,000\text{-}11,000$ K can be identified with the WNM. This agrees with Mebold (1972), Verschuur and Smeltz (1989), Verschuur and Magnani (1994), Verschuur and Peratt (1996), and Haud and Kalberla (2007). Thus, like most previous

Gaussian deconvolution studies, our data shows the presence of components with linewidths corresponding to the CNM and the WNM.

The nature of the broad component (BC) at ≈ 40 km/s is much less obvious than the other components. Unlike previous studies, we can state that the existence of the BC in our data is almost surely not to be due to instrumental effects because of the low side lobe response of the GBT. Thus, this feature is almost surely “real”, though its line width cannot be attributed to temperature only. We now explore several alternatives for its origin.

The BC could be made up of a superposition of CNM features along the line of sight. If $\sigma_v(\text{standard cloud}) = 1.6$ km/s, $\sigma_v(\text{BC}) = 40$ km/s, and we let n be the number of clouds along the line of sight, $n(1.6)^2 = (40)^2$ predicts that the superposition of approximately 600 clouds would be necessary to produce this feature. Spitzer estimates that there are 6.2 of these clouds per kpc, so our line of sight would need to be 100 kpc long to encompass that many clouds. Thus, the BC cannot solely be a superposition of CNM features.

A portion of the BC could be due to the WNM. If this were the case,

$$\sigma_v^2(\text{BC}) = \sigma_v^2(\text{WNM}) + \sigma_v^2(\text{other}).$$

With values of $\sigma_v(\text{BC}) = 40$ km/s and $\sigma_v(\text{WNM}) = 15$ km/s, $\sigma_v(\text{other}) = 37$ km/s. This width corresponds to a temperature of 55,000 K, which is still unphysical.

The BC could be a superposition of WNM regions along the line of sight. Using the same logic as for the superposition of CNM clouds along the line of sight, $n(15)^2 = (40)^2$. Solving for n predicts that 7 WNM features would need to be superimposed to produce the BC, which is unlikely given that the extent of a WNM region should be longer than a CNM region because of the lower density of the WNM versus CNM (0.3 vs. 30 cm⁻³). However, it is not impossible that

there could be several distinct WNM regions along a line of sight since the WNM has a larger filling factor than the CNM.

The most likely of these scenarios is that the BC could be produced by a combination of streaming motions, which are systematic gas motions coherent over length scales of a kpc or larger. They are induced by major mass concentrations attracting HI gas gravitationally. They can be seen on a rotation curve of the Galaxy as deviations from a smooth line fit to the terminal velocities in HI data (e.g., Burton and Gordon 1978). Their velocity extent is ± 7 km/s compared to the Galactic rotational velocity at that point, corresponding to a σ_v of ≈ 6 km/s. In addition to streaming motions there exist noncircular motions of the streamlines of the Galaxy. Their typical velocity extent is ± 10 km/s corresponding to $\sigma_v \approx 8.5$ km/s (Blitz and Spegel 1991). Thus, if we add both streaming motions and noncircular motions to the CNM and WNM features we obtain the relationship

$$\sigma_v^2(\text{BC}) = n_1 \sigma_v^2(\text{CNM}) + n_2 \sigma_v^2(\text{WNM}) + \sigma_v^2(\text{SM}) + \sigma_v^2(\text{NC}).$$

Using the values for the velocity dispersions used previously and setting $n_1 = n_2$ (i.e. saying that each CNM cloud is surrounded by one WNM envelope), $n = 6$. This is consistent with the distribution of Spitzer's "standard clouds".

The simplest explanation for the width of the BC is that it is a superposition of CNM, WNM, streaming motions, and noncircular motions along the line of sight. The width of the BC component can be reproduced in a straightforward manner by using typical parameters for the various components.

CHAPTER 6

CONCLUSION

We have de-convolved over 5,000 HI spectra at 21cm from the 100 meter Green Bank Telescope into Gaussian components using the xgaussfit program in IDL. The Green Bank Telescope is ideal for studying the distribution of atomic hydrogen because of its innovative design; the off-axis feed arm does not shadow the dish and so the side lobe response of the telescope is very low. Thus the resulting HI profiles are among the cleanest ever obtained. Each spectrum has from 2-8 HI components, each of which are fit by a Gaussian profile in the manner described both verbally and pictorially in Chapter 2.

Histograms of the number of components vs. velocity and area vs. velocity show features at $\approx 3\text{-}4$ km/s, $\approx 10\text{-}17$ km/s and ≈ 40 km/s corresponding to temperatures of 360-640 K, 4,000-11,000 K, and 64,000 K, respectively. The first 2 features have been seen before (see, e.g., Verschuur and Magnani 1994). The 360-640 K feature can be identified with the CNM and the 4,000-11,000 K feature can be identified with the WNM, confirming the previous work of Mebold (1972), Verschuur and Magnani (1994), and Haud and Kalberla (2007). However, in addition to these already known components, a very broad component is detected in the spectra. If the width of the feature is interpreted in terms of a kinetic temperature, then the resulting temperature is unphysical: $\geq 60,000$ K. The BC, previously suspected to be instrumental, is seen clearly in our data and, given the clean GBT beam, is likely real. The BC is likely produced by a combination of CNM features, WNM features, and Galactic streaming and noncircular motions.

Future studies in this field should concentrate on studying the spatial distribution of the BC. Although it is likely that the BC is made up of well known phenomena (e.g. CNM, WNM), if our interpretation that Galactic streaming motions and noncircular motions contribute to the broadening, then distinct spatial patterns should be recognizable as observations are made along or through spiral arms. While these studies may not provide new information on the phases of the cold atomic gas component of the Galaxy, they may reveal new, more detailed information about how the Galaxy's rotation deviates from the idealized models.

REFERENCES

- Bahcall, J.N., 1983, APJ, 267, 52
- Bakes, E. L. O. and Tielens, A. G. G. M. 1990, ApJ, 365, 620
- Combes, F. 1991, ARAA, 29, 195
- Cox, D.P. 2005, ARAA, 43, 337
- Goldsmith, P. F. 1987, Interstellar Processes, 51
- Kulkarni and Heiles, 1988, Galactic and Extragalactic Radio Astronomy 2nd ed, 95
- Lepp, S., Dalgarno, A. 1988, ApJ, 335, 769
- Low F. J. et al 1984, ApJ, 278, L19?
- Payne, H. E., Salpeter, E. E., and Terzian, Y. 1983, ApJ, 272, 540
- Raley, E. A., Shelton R. L., Plewa T. 2007, ApJ, 661, 222
- Reynolds, R.J. 1987, A.J., 323, 118
- Sanders, D. B., 1984, APJ, 276, 182
- Savage, B. D., Massa, D., 1987 ApJ 314 (1987), p. 380.
- Scoville N. Z., 1987, Interstellar Processes, 21
- Spitzer, L. Jr. 1978, Physical Processes in the Interstellar Medium (New York: John Wiley and Sons)
- Tielens, A. G. G. M. 2005, The Physics and Chemistry of the Interstellar Medium (Cambridge University Press)
- Wakker, B.P. 1991, ARAA, 35, 47
- Werner, M., Fazio, G., Rieke, G., Roellig, T.L., and Watson, D. M., 2006, ARAA, 44, 269
- Whittet, D. C. B., 2003, Dust in the Galactic Environment 2nd ed., (Bristol IOP)
- Verschuur, G. L., Magnani, L., 1994, A.J., 107, 287
- G. L. Verschuur and A. L. Peratt, 1999, A.J., 118, 125